UiT The Arctic University of Norway

Faculty of Fisheries, Biosciences and Economics, Department of Arctic and Marine Biology

APPLICATION OF AN UNDERWATER HYPERSPECTRAL IMAGER (UHI) FOR THE STUDY OF SEA ICE ALGAE

Analysis of sea ice algal chlorophyll *a* biomass distribution and production using hyperspectral imaging

Janina Osanen

Master's thesis in Biology BIO-3950, August 2022

1. ABSTRACT

Sea ice provides an important habitat for sea ice algae, the main primary producers in sea ice covered ocean areas. In order to reliably estimate sea ice algal distribution and production, it is important to develop remote sensing methods that can provide these estimates with minimal disturbance from ice coring. Underwater hyperspectral imagers (UHI) can capture fine-scale variability in the transmitted spectral profile directly below the sea ice-water interface, which then can be related to ice core-derived chlorophyll *a* (chl *a*) concentration, providing estimates of *in situ* chl *a* biomass across spatial scales. The main aim of this research was to obtain optimal Normalised difference index (NDI) wavelength combinations for *in situ* and *in vivo* surveys using the two different approaches of standardized radiance and transmittance, and to then apply the resultant model for mapping fine scale (mm) chl *a* distribution. Results indicated successful application of laboratory-based NDI-combinations for estimating fine-scale chl *a* biomass variability. Combining the model with O_2-based laboratory experiments, fine scale differences in net community production relative to chl *a* were also estimated for UHI surveys from two contrasting Svalbard fjords, Tempelfjorden and Van Mijenfjorden. Additionally, the effect of accessory pigments, with a focus on fucoxanthin, on bio-optical models was investigated.

CONTENTS

2. CHAPTER 1: INTRODUCTION

2.1 CONTEXT

Sea ice covers around 10 % of the world's oceans areas and is an important feature of polar ocean from a biological, chemical, economical and political perspective (Lund-Hansen *et al.*, 2020b). It provides a habitat for sea ice algae, which are microscopic photosynthetic organisms living within the ice, that can account for up to 60 % of total primary production in the Arctic (Fernández-Méndez *et al.*, 2015). Climate change is causing a rapid decrease in Arctic sea ice extent, with consequences that will reach global scales. With decreasing sea ice cover and thinning of the ice, the habitat for sea ice algal related primary production is changing, but the direction is still uncertain. The monitoring sea ice algal biomass and the response to changes in the environmental conditions is restricted by logistical challenges as well as the lack of non-invasive and representative sampling methods. The development of new monitoring techniques is essential, as they could provide means of estimating the response of sea ice algae to a rapidly changing environment and its regional and global consequences.

2.2 OBJECTIVE

The overarching goal of this thesis was to assess the potential of an Underwater Hyperspectral Imager (UHI) for studying different aspects of sea ice algal characteristics, such as chl *a* biomass and pigment concentration, as well as net community production. This study applies the bio-optical model of Normalised difference indices (NDI), developed by Mundy et al. (2007), and determines the optimal wavelength combinations for experimental cultures and natural fjord systems. The thesis has two main objectives:

1) Determining the best approach for obtaining optimal NDI wavelength combinations for experimental and natural communities for estimating fine-scale variability of chl *a* biomass.

2) Assessing the applications of the optimal NDI model for estimations of fine-scale net community production and accessory pigment composition, particularly focusing on fucoxanthin.

2.3 THESIS STRUCTURE

In addition to this introduction section, three other chapters are included. Chapter one provides a review of central concepts needed to understand sea ice as a habitat for algae. The structure of sea ice and its influence on incoming solar radiation, in terms of reflectance, scatter and absorption, is presented before reviewing sea ice as a habitat for sea ice algae. The effect of algae on transmitted light as a result of pigment absorption is reviewed, as this is an essential concept for understanding the bio-optical models used in this study. The main objective of chapter two is the application of such bio-optical models in experimental and *in situ* conditions. There, standardized radiance and transmittance are related to measured chl *a* to determine the optimal model for estimating chl *a* biomass distribution using a UHI. This chapter is compiled into a manuscript and will be submitted to *Journal of Geophysical Research: Oceans.* The third chapter explores the potential of bio-optical models, combined with laboratory incubations, for estimating fine-scale net community production. In addition, the potential for identifying and quantifying sea ice algal accessory pigments using a UHI is investigated. Chapter four is a conclusion chapter, summarizing the conclusion of the thesis and future work suggested. A list of abbreviations used in the thesis is included after this section.

2.4 REFERENCES

Fernández-Méndez, M. *et al.* (2015) 'Photosynthetic production in the central Arctic Ocean during the record sea-ice minimum in 2012', *Biogeosciences*, 12(11), pp. 3525–3549.

Lund-Hansen, L.C. *et al.* (2020) 'The Book, and Ecology of Sea Ice', in L.C. Lund-Hansen et al. (eds) *Arctic Sea Ice Ecology: Seasonal Dynamics in Algal and Bacterial Productivity*. Cham: Springer International Publishing, pp. 1–12. Available at: https://doi.org/10.1007/978-3-030-37472-3_1.

3. LIST OF ABBREVIATIONS

Chl *a*	Chlorophyll *a*
PAR	Photosynthetically active radiation
FYI	First-year sea ice
MYI	Multi-year sea ice
UHI	Underwater Hyperspectral Imager
NDI	Normalized difference index
ASW	Artificial seawater
NCP	Net community production
VMC	Van Mijenfjorden mixed community
ATT	*Attheya* sp.
EUC	*Eucampia groenlandica*
COMB	VMC + EUC + ATT cultures pooled

4. CHAPTER 2: BACKGROUND

The Arctic Ocean is an extreme environment that nonetheless sustains a range of organisms, from the microscopic to megafauna. The sea ice covering the Arctic Ocean is a multi-phase habitat of ice, gas and liquid brine that provides shelter for invertebrates and space for microbial assemblages like algae to grow, which in turn support higher trophic levels. Sea ice algae, together with pelagic phytoplankton, are the main primary producers in ice-covered ocean waters and therefore, they form the base of the food web in the Arctic. The complex structure of sea ice has a direct effect on the transmittance of light, which in turn strongly affects the growth of sea ice algae within the ice. This section of the thesis document will provide background information about the structure of sea ice, the impact of sea ice structure on light transmittance through the ice, as well insight on how subsequent variability in light transmittance impacts sea ice algal growth and distribution. The background will also provide insight how algal absorption within the ice in turn impacts the spectral profile measured beneath the ice. Current and state-of-the-art techniques remote sensing will be discussed, particularly those focused on using transmitted irradiance to remotely study ice algal blooms. In turn, his lays the groundwork for the methods developed within this thesis associated with use of an Underwater Hyperspectral Imager (UHI).

4.1 THE ARCTIC SEA ICE AND CLIMATE CHANGE

The Arctic is characterized by strong seasonal variation in sea ice extent and light availability in the ocean. Arctic sea ice reaches its maximum extent around April and its minimum in September, although the timing of these extents is subject to considerable interannual variability (Peng and Meier, 2018). This is a result of variability in winds and ocean currents, as well as regionally variable oceanic heat fluxes (Haas, 2017). Furthermore, climate change is most pronounced in the Arctic, as the area is warming at twice the rate of the rest of the globe (Meredith *et al.*, 2019).The most evident decline in sea ice extent occurs particularly in summer and autumn, at the end of the melt season. Based on satellite observations ranging from 1979 up until today, the lowest sea ice extent on satellite record was observed in 2012 (Parkinson

and Comiso, 2013) and the second-lowest in 2020 (Liang *et al.*, 2022). In addition to a lower percent of sea ice cover, the thickness and age of the ice are also changing. Here, thinner first-year sea ice (FYI) is replacing the thicker and older multi-year sea ice (MYI), which is disappearing from the Arctic Ocean due to enhanced melt and greater drift of the ice out from the High Arctic (Kacimi and Kwok, 2022).

4.2 SEA ICE FORMATION AND STRUCTURE

Sea ice has a unique structure due to the presence of salts in the water that are expelled from the crystal matrix during ice formation, which in turn give rise to its complex structure (Petrich & Eicken, 2017). The expelled salts known as brine become concentrated into channels and pockets within the ice matrix and form an extensive network within the ice.

As seawater reaches the freezing point of -1.84°C, ice crystals start forming, creating a thin layer of frazil ice. These ice crystals tend to form aggregates and consolidate into a slushy layer at the ocean surface. In calm and turbulent waters, a layer of nilas and pancake ice form, respectively (Petrich and Eicken, 2017). Nilas ice is the result of thermodynamic growth of sea ice, where the ice thickens as water freezes at the ice-ocean interface (Weeks and Ackley, 1986; Naumann *et al.*, 2012). Thermodynamic growth of ice therefore takes place in the bottommost part of the columnar layer at the ice-ocean interface, where the ice crystals are separated by the brine layers and form a fragile structure called the skeletal layer (Petrich and Eicken, 2017).

Sea ice is characterized by strong vertical gradients in temperature, salinity and nutrient concentrations. As discussed earlier, the unique structure of sea ice is attributed to rejected salt ions during formation, but it is the combination of temperature and salinity that determines the structure and properties of the ice (e.g., porosity). The temperature of the ice at the surface is close to the atmospheric temperature, depending on the presence or absence of a snow cover and its thickness, as the snow acts as an insulating layer at the ice-air interface (Perovich and Elder, 2001). There is typically an increase in temperature towards the bottom of the ice, and the temperature at the ice-water interface is close to the freezing point of sea ice (Arrigo, 2014). The shape of the gradient is, however, affected by numerous factors, such as rapid changes in atmospheric temperatures, surface flooding events (where the weight of the snow pushes the ice below the sea surface) and rafting of ice floes (Petrich and Eicken, 2017). The gradient of the bulk salinity, i.e., total salinity of the ice and brine, typically follows a C-shape in young

FYI until desalination during the summer melt season alters the shape in the uppermost parts of the ice (**Fig. 1**).

The brine volume fraction in the ice is determined by the temperature and bulk salinity, which in turn determine the permeability of the sea ice. Sea ice is considered permeable at the threshold of -5 °C, 5 ppt salinity and a volume fraction of 5 % (Golden, Ackley and Lytle, 1998). Ice with high salinity and high temperature has a larger brine volume and is therefore more permeable than lower salinity ice with low temperatures.

As a result of these processes, the top layer of sea ice is granular in structure, with randomly aligned ice crystals (**Fig. 1**). This layer is followed by a columnar layer, which is characterized by sub-millimetre thick but elongated ice crystals with a horizontal alignment. These crystals may reach a length of up to 40 cm and in between these crystals are narrow films of brine.

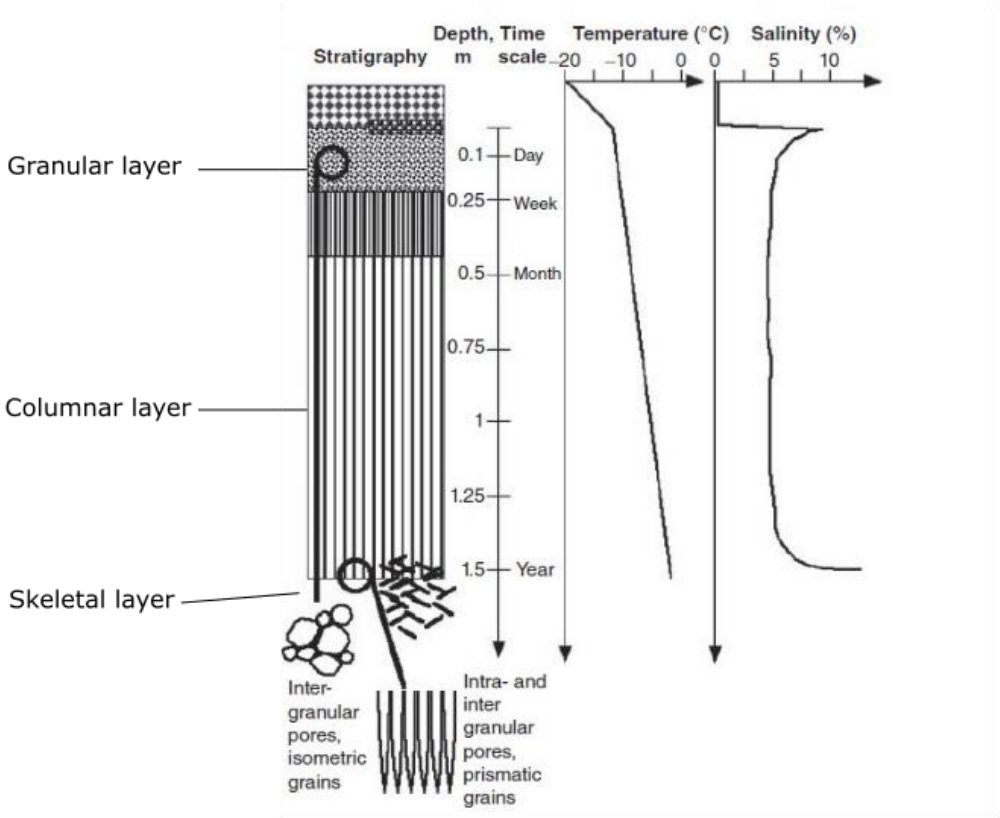

Figure 1. Schematic illustrating the main structures and typical temperature and salinity gradients for first year sea ice. Modified from Petrich & Eicken, 2017.

Seasonally, sea ice melt begins with increasing atmospheric temperatures and high irradiance levels. Rising temperatures change the microstructure of the ice through enlarging brine channels, thus increasing porosity and connectivity within the ice (Petrich and Eicken, 2017). Brine drainage due to meltwater leads to desalination of the ice, and as the melted sea ice has a lower salinity than the seawater below, and therefore lower density, the meltwater accumulates at the bottom and on top of the ice, forming melt puddles and ponds.

4.3 RADIATIVE TRANSFER

The radiation from the sun comprises of wavelengths within the range of 250 to 2500nm of the electromagnetic spectrum. The focus of this thesis will mostly focus on visible light (400-750nm), particularly the range of photosynthetically active radiation (PAR, 400-700 nm). The complex structure of sea ice and the inclusions within affect the magnitude, direction and spectral profile (i.e. wavelengths) of the light that enters the media and is then transmitted to the ice-water interface and ocean water below. Radiative transfer describes the propagation of light through a medium, such as sea ice, with a random distributions of scatterers (Marzano, 2014). The part of the incident solar radiation that is not reflected at the surface is subject to scattering or absorption of the ice and its inclusions, and the remaining radiation is transmitted to the ocean. Scattering and reflectance of light interacting with ice, and particularly snow, mostly affect the magnitude of visible light, while the spectral profile is primarily influenced by absorbing inclusions, such as brine, air bubbles and biota within the ice (Perovich, 2017). Radiative transfer theory of sea ice is still limited, as absorption and scattering of light is difficult to measure and quantify form beneath the ice. Models used range from the simple equations of exponential decay to models that include numerous parameters, such as the temperature of the ice and the optical properties of individual inclusions (Light, Maykut and Grenfell, 2004; Ehn, Mundy and Barber, 2008; Perovich, 2017).

Albedo is the ratio of incident radiation that is reflected or backscattered into the atmosphere. It is a central concept in ice- and snow-covered areas, as the albedo-temperature feedback affects the temperature of the area (Box *et al.*, 2012). Albedo has values between 0 and 1, where no light is reflected at 0 albedo and the latter reflecting or backscattering all incoming light.

Thick and dry snow on sea ice has the highest albedo of visible wavelengths with values up to 0.95 (Perovich, 2017), while wet snow shows considerably lower but variable values between 0.7-0.75 (Brandt et al., 2005; Perovich & Polashenski, 2012). Growing snow grain size also causes a slight drop in albedo, but the effect is weaker than the effect of wet snow (Perovich et al., 2002). Albedo increases substantially during melt season, as forming melt ponds and puddles creates a mosaic of variable albedo patches across the sea ice (**Fig. 2**). Albedo can show notable differences between ponds, as values between e.g. 0.15 and 0.55 have been recorded within the same area (Perovich, 2017).

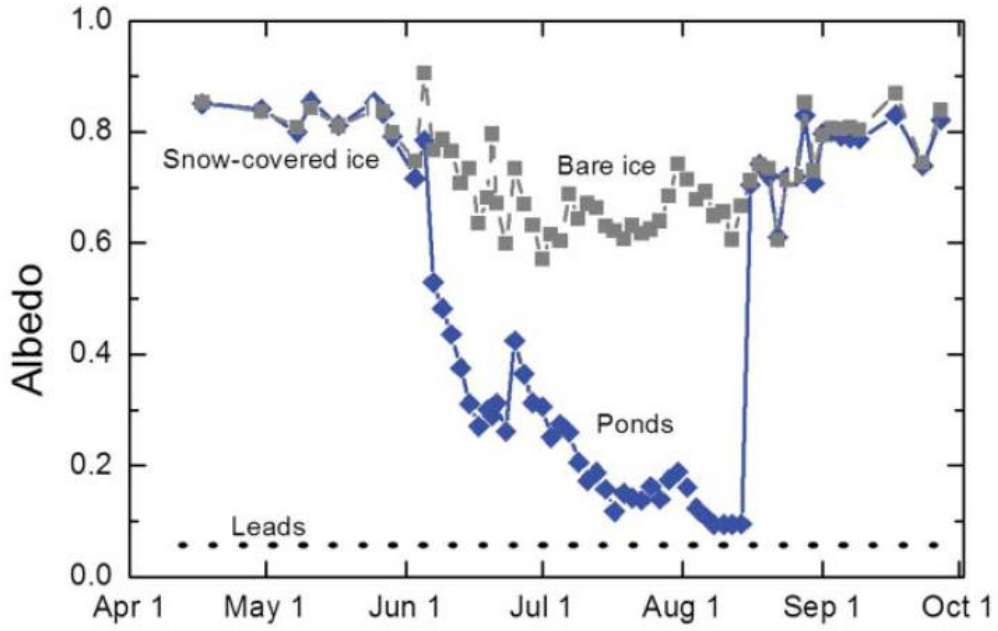

Figure 2. Seasonal evolution of albedo for bare MYI and ponded ice (Perovich *et al.*, 2002; Perovich, 2017).

Scattering is the result of the differences in the index of refraction between two materials; larger differences result in stronger scatter. Sea ice includes a high number of scatterers with different scattering coefficients, making direct measurements of scattering in sea ice complicated (Perovich, 2017). It can, however, be estimated through a model that includes the microstructure of the ice itself as well as the individual scatterers, such as gas, brine and solid salts within the ice (Light et al., 2004). The attenuation of light in the snow is dominated by scattering, while both scattering by ice crystals and absorption by inclusions dominate in sea ice (Mundy et al., 2007)

Scattering coefficients vary between the different layers of the ice, as the microstructure of ice varies between layers. In addition, scattering of sea ice may increase as the melt season progresses and the microstructure of the ice changes. For example, brine drainage creates a higher fraction of air within the ice, which has a higher scattering coefficient than the surrounding ice (Katlein, Nicolaus and Petrich, 2014).

Scattering in sea ice is predominantly forward scattering (i.e. downwards), resulting in minor change in the direction of the light originating from the sun (Perovich, 2017). It is, however, important to consider the heterogeneity of sea ice on the scattering coefficient. For example, the length and orientation of the ice crystals on a microscopic scale (Nghiem *et al.*, 1995), and larger structural differences, such as ridges and melt ponds all affect the scattering within the ice as a consequence of different scattering coefficients (Katlein, Nicolaus and Petrich, 2014).

As light attenuation in pure sea ice is mostly caused by scattering, ice alone has minimal effect on the distribution of light wavelengths. Light absorbing inclusions include both biological and non-biological materials. In sea ice biological materials mainly includes Colored Dissolved Organic Matter (CDOM) and pigments of sea ice algae (see Section 4.5). The CDOM, which can either be autochthonous, i.e., biological, or allochthonous, when it is from a terrestrial source, exhibit slightly overlapping absorption within the blue light area. The absorption of CDOM, however, is strongest near the ultraviolet (UV) radiation and decreases exponentially in the blue light area (**Fig.3**) (Babin *et al.*, 2003; Johnsen *et al.*, 2011).

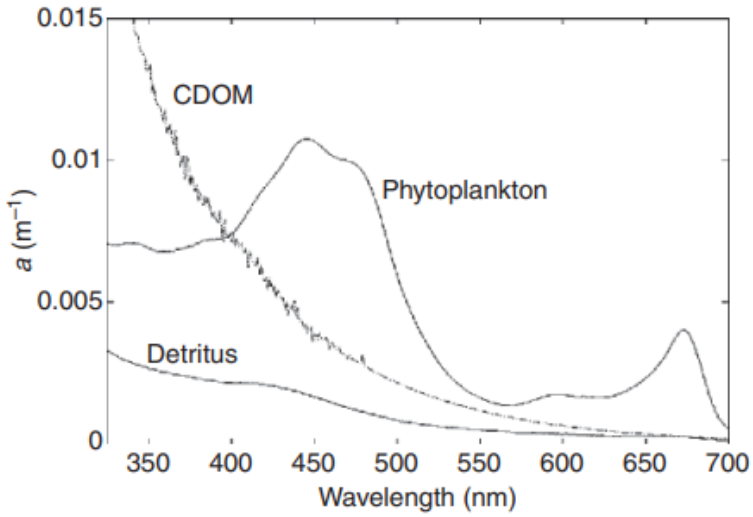

Figure 3. Comparison of absorbing components in seawater (Johnsen *et al.*, 2011)

4.4 SEA ICE AS A HABITAT

While bacteria are found in all parts of the ice, most ice algae reside in the bottommost 20 cm where environmental conditions, such as light, temperature and salinity are suitable and nutrient concentrations sufficient for growth (Arrigo, 2017). Occasionally, ice algae may be found in the internal layers of sea ice, generally at the freeboard level, where seawater can infiltrate the ice and provide sufficient nutrients to sustain an internal community (Arrigo, 2017). Surface layer communities are often a result of flooding events on thin ice, where the weight of the snow leads to flooding by seawater at the snow-ice interface, which is typical in Antarctic sea ice (Meiners *et al.*, 2012).

Organisms are incorporated from the water column into the ice matrix during ice formation, a process that has been shown to favour larger cell sizes or properties of the surface of the cell that aid with the incorporation (Gradinger & Ikävalko, 1998). Diatom species, such as e.g. pennate diatoms *Nitzschia frigida*, *Navicula* spp. and centric diatoms *Thalassisosira* sp., are some of the most common ice algae found in the Arctic (Horner and Schrader, 1982; Leu *et al.*, 2015). These species grow within or attached to the ice and are rarely found in the water column (Leu et al., 2015 and references therein).

Algae can utilize light within the range of PAR, which falls within the range of 400-700 nm. Light and nutrients are the dominant limiting factors of algal growth in the Arctic, light often being the limiting factor in early spring and nutrients at the later stages of the bloom (Leu *et al.*, 2015; Arrigo, 2017). The onset of the bloom occurs as soon as there is enough light available for shade-adapted algae to grow in the bottommost centimetres of the ice (Leu *et al.*, 2015). Towards summer, light and temperatures steadily increase, altering the microstructure of the ice and increasing the drainage of brine and nutrients (Lund-Hansen *et al.*, 2020).The timing of the onset and termination of the bloom is strongly affected by the thickness of the snow cover, due to its strong albedo and effect on light attenuation, as well as its isolating properties. A thick snow cover may delay the start of the bloom by reflecting the majority of incoming solar radiation, while it may prolong the bloom by preventing rapid ice melt and protecting the algae from harmfully high irradiance (Campbell *et al.*, 2015; Leu *et al.*, 2015).

Macronutrients, such as dissolved inorganic nitrate (NO_3^-), nitrite (NO_2^-), ammonium (NH_4^+), phosphate (PO_4^{3-}) and silicic acid ($Si(OH)_4$), are inorganic compounds that algae require for growth. As the nutrient concentrations in sea ice are often much lower than those recorded in the water column, sea ice algae can be limited by nutrient availability, particularly in times of high algal production (Meiners and Michel, 2017). Silicic acid is especially important in sea ice, as the main taxonomic group in sea ice are diatoms that form shell-like frustules of silica. Nutrient availability often governs the vertical distribution of biomass, therefore the highest algal biomass concentrations are measured in the bottom centimeters of the ice (Arrigo, 2017). Therefore, even if near-surface communities have sufficient light conditions, they are often nutrient limited, unless a flooding event has occurred.

Algal production and growth are subject to variability due to changing growth conditions, such as shifting light intensity, nutrient availability and salinity (Lund-Hansen et al., 2020; Ralph et al., 2007; Yoshida et al., 2021). The changes in production, often measured and modelled through photosynthetic efficiency and maximum photosynthetic rate, are, together with a change in pigment concentration, an acclimatisation response to a changing environment (Cota and Horne, 1989). As sea ice is a dynamic habitat for sea ice algae, which experience large fluctuations in light intensity as well as nutrient availability. The rate of production relative to chl *a* is therefore not constant, but prone to notable spatial and temporal variability (Campbell, Lange, *et al.*, 2022). The photosynthetic processed are often modelled through photosynthesis-irradiance curves (PI), which assesses the photophysiological responses to changing irradiance levels.

4.5 PIGMENTS

As photosynthetic organisms, algae require light for growth, and the light is absorbed by the cells using a suite of specialised lipid-protein compounds known as pigments. The main photosynthetic pigments in diatoms are chlorophylls chl *a*, chl c and the carotenoid fucoxanthin. Chlorophyll *a* (chl *a*) is the primary light-harvesting pigment, with the main absorption peak around 440 nm (blue light) and a secondary peak of 665-675 nm (red light). In addition to chl *a* there are a number of accessory pigments found within algae, such as fucoxanthin and

chlorophylls b and c, which expand the absorption spectra by harvesting wavelengths outside of the chl *a* (**Fig. 4**) This allows for the effective utilization of different wavelengths in variable light conditions, which is particularly important in a dynamic sea ice environment. Carotenoids more commonly function as photoprotective pigments, preventing cell damage at high irradiance levels. The standard carotenoids in diatoms are fucoxanthin, diadinoxanthin, diatoxanthin and β,β-carotene (Jeffrey, Wright and Zapata, 2011), while violaxanthin, antheraxanthin and zeaxanthin have been documented in high light environments (Jeffrey, Wright and Zapata, 2011; Kuczynska, Jemiola-Rzeminska and Strzalka, 2015).The ratio of different pigments depends on community composition and the effect of environmental conditions on individual cells as they acclimatize to the changing light conditions (Jeffrey, Wright and Zapata, 2011; Alou-Font E *et al.*, 2013; Galindo *et al.*, 2017).

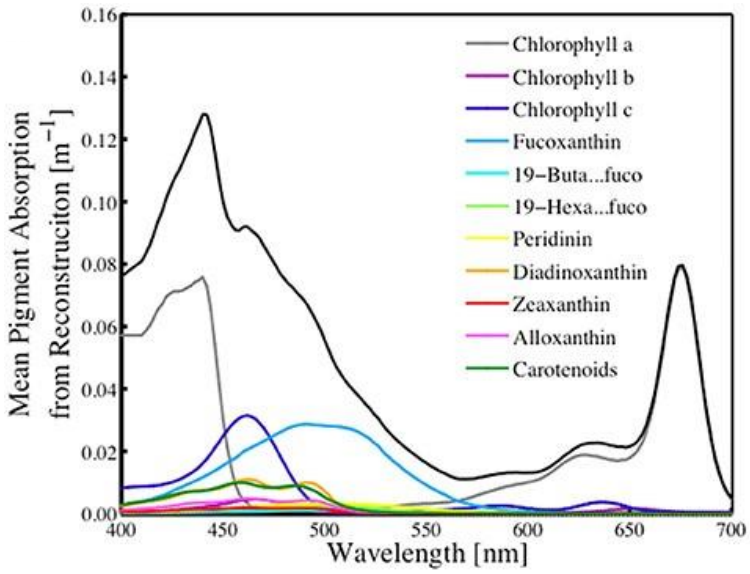

Figure 4. Pigment-specific absorption of main pigments found in phytoplankton. Black solid line shows total absorption by all pigments (Moisan *et al.*, 2017).

4.6 BIOMASS SAMPLING TECHNIQUES

Assessing the growth of sea ice algae using traditional ocean colour-based remote sensing technologies is limited in ice covered regions. Traditionally (i.e. for pelagic phytoplankton), the main photosynthetic pigment chl *a*, which can be identified through remote sensing due to its reflection of certain wavelenghts, is used as a proxy for sea ice algal biomass. There are several methods for the collection and measurement of chl *a* in sea ice. Ice coring is a standard method for physical sampling, and the cores are then melted in filtered seawater and the melted sample is processed by filtering and placing the filter into acetone for extraction of pigments. The concentration of chlorophyll *a* can then be estimated by e.g. fluorometry or spectrophotometry. In both methods, two measurements are taken – one of the extracted pigment solution and another measurement after the addiction with an acid, such as hydrochloric acid (HCl) (Lorenzen, 1967; Parsons, 1984).

A fluorometer quantifies the amount light emitted by the extracted pigment following excitation, and this reading can be converted to concentration of chlorophyll *a* (e.g. mg m^{-3}) following the equation presented in (Parsons 1984). Spectrophotometry is based on measuring the absorbance and emission of light by the material before and after acidification with e.g., HCl, at specific wavelengths (750 nm and 665 nm for chl *a*). The concentration of Chl *a* is then calculated using the equation determined by (Lorenzen, 1967)

Ice coring is time consuming, destructive, and limited in its ability to capture the spatial distribution of sea ice algae. Due to the destructiveness of the method, coring prohibits time-series studies and may lead to a considerable loss of sample, particularly for ice with a fragile skeletal layer and only lightly attached algae (**Fig. 6**).

Ice algal biomass distribution is characterized by patchiness across spatial scales – from differences over millimetres to several kilometres (Granskog *et al.*, 2005; Lange, Katlein, *et al.*, 2017; Lund-Hansen *et al.*, 2017; Forrest *et al.*, 2019). This variability can be attributed to differences in ice structure (e.g. brine channels), and at the larger scale, differences in the physical properties of the ice (e.g. ridges and hummocks; Lange et al., 2017a) and a variable distribution of snow (Gosselin *et al.*, 1986; Meiners *et al.*, 2017; Lange *et al.*, 2019). Small-scale differences across the skeletal layer have also been recorded, and although not certain, surface roughness of the ice-water interface and the distribution of brine channels have been

suggested to be key drivers (Mundy *et al.*, 2007; Lund-Hansen *et al.*, 2017). The high degree of spatiotemporal variability of ice algal biomass highlights the limitations of ice coring as a method for mapping ice algal biomass distribution. Coring, as a point measure, only provides snapshots of the ice algal bloom and its dynamics, leading to uncertainties of the true magnitude of the bloom.

Seasonally, structural changes of the ice during melt season (Leu *et al.*, 2015) cause large seasonal variability of biomass, with the highest biomass typically recorded in spring when there is enough light and the algal growth is not yet limited by nutrient availability (Lavoie, Denman and Michel, 2005; Leu *et al.*, 2015). Short scale temporal variability related to differences in the snowpack have also been recorded, which adds onto to the dynamic distribution of biomass (Juhl and Krembs, 2010; Lund-Hansen *et al.*, 2014; Campbell *et al.*, 2015; Cimoli, Meiners, *et al.*, 2017).

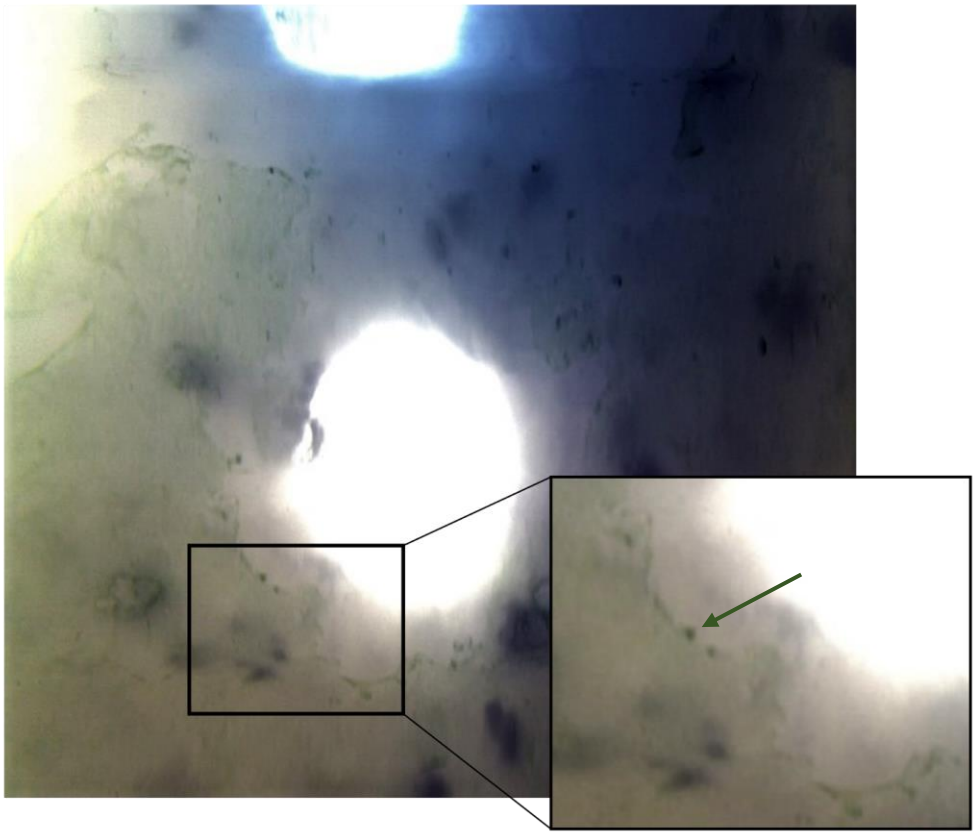

Figure 6. Loss of sample by coring in Tempelfjorden, Svalbard in April 2021. There is a clear absence of algae (green arrow) around the cored area.

4.7 TRANSMITTED IRRADIANCE AND REMOTE SENSING

Ocean color data by satellite observations is used for estimating pelagic phytoplankton blooms, but the same technology cannot be directly applied to ice-covered areas. Due to the limitations of ice coring, there is a growing interest for the development of non-invasive methods that can capture the spatiotemporal variability of ice algal biomass distribution. Under-ice remote sensing technology based on measuring the spectral composition of transmitted light through the ice is becoming increasingly prominent in sea ice algal research (Cimoli, Meiners, *et al.*, 2017). Promising results have been obtained by deploying upwards looking irradiance sensors under the ice for measuring ice algal biomass and production (C. J. Mundy *et al.*, 2007; Campbell *et al.*, 2015; Cimoli, Meiners, *et al.*, 2017; Lange *et al.*, 2019; Campbell, Lange, *et al.*, 2022).

Based on the wavelength-specific absorption of algal pigments, sea ice algal biomass can be estimated by changes of the spectra caused by the light absorption by algae. Irradiance sensors used by e.g., Legendre and Gosselin (1991) have laid the groundwork further development of using transmitted irradiance to estimate biological parameters. Estimating biomass through the linear relationship between certain wavelengths and biomass is possible by calibrating the transmitted irradiance measurements with samples of chl *a* collected through coring. Evidence of a relationship between transmitted irradiance and chl *a* concentration was first provided by Legendre and Gosselin, 1991 where they used a ratio between two wavelengths (540 nm and 671 nm) of low and high chl *a* absorption to characterize chl *a* concentration. Further developments have been made later by the introduction of normalized difference indices of specific wavelengths for characterizing chl *a* (Mundy *et al.*, 2007), a method that has been applied for several different regions with promising results (Campbell et al., 2022b and references therein).

The relationship between measured irradiance and chl *a* can be described by calculating Normalized difference indices (NDIs) of specific wavelengths correlated to measured chl *a* (Mundy *et al.*, 2007; Campbell *et al.*, 2015). NDIs are calculated according to the following equation:

$$NDI = [T(\lambda 1) - T(\lambda 2)] / [T(\lambda 1) + T(\lambda 2)],$$

where T(λx) represent transmittance at a given wavelength within the photosynthetically active radiation region (PAR, 400-700 nm). Two wavelengths are compared in order to characterize the biomass using irradiance ratios as NDI values between values -1 and +1 (C. J. Mundy *et al.*, 2007). Several different wavelength combinations have recently been used for determining sea ice algal biomass in different regions of the Arctic and Antarctic, most of them within the range of 410 nm and 490 nm (**Fig. 7**), which is in close proximity to the primary absorption peak of chl *a* (Campbell *et al.*, 2022). There have also been studies reporting combinations near the second absorption peak, around 670 nm (Campbell *et al.*, 2015; Wongpan *et al.*, 2018), which can be used in regions with a thin snow cover. Calibrating the relationship between transmitted light and chl *a* concentration for a particular region is advised, as there may be regional differences between the non-biological absorbents in sea ice as well as the concentration of accessory pigments of algae (Campbell *et al.*, 2022).

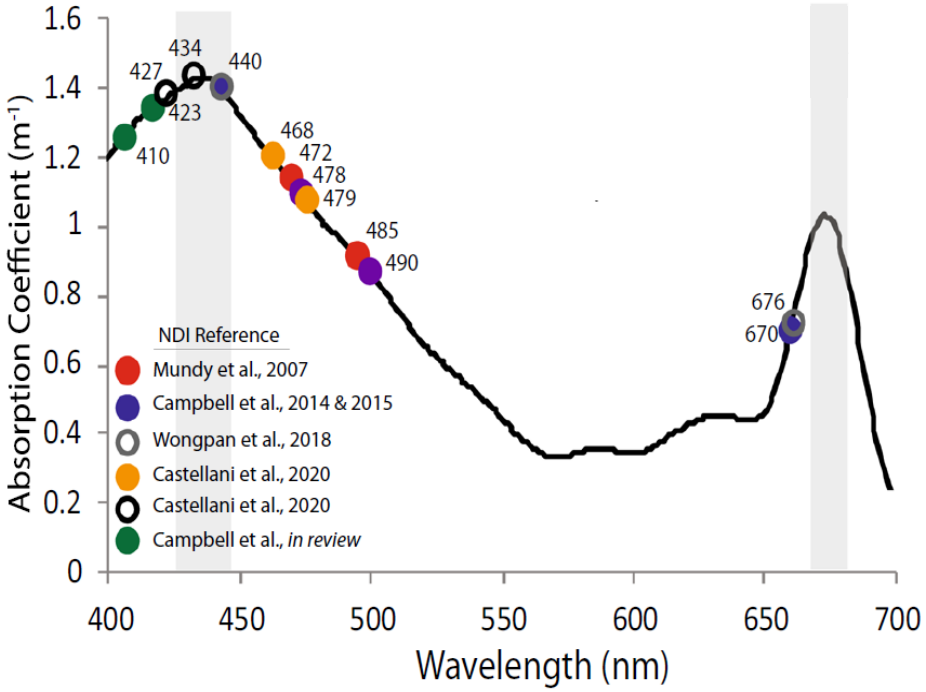

Figure 7. Summary of published NDI combinations. The areas of chl *a* absorption are highlighted in grey (Campbell *et al.*, 2022).

Further underwater remote sensing methodologies for use of estimating ice algal biomass have been developed using upward facing hyperspectral sensors and imagers deployed under the ice (Cimoli *et al.*, 2019; Wongpan *et al.*, 2020). Hyperspectral imagers measure radiation across the electromagnetic spectrum and provide high resolution spectral information across spatial scales, unlike irradiance and radiance sensors which have a much wider footprint (Cimoli, Lucieer, *et al.*, 2017). Underwater hyperspectral imagers (UHI) have only recently become available for use in marine research, and promising results have been obtained when applying the technology for e.g. mapping the seafloor (Johnsen *et al.*, 2016; Mogstad, Johnsen and Ludvigsen, 2019). Cimoli et al. (2019) deployed an upwards facing UHI on a sliding platform under the sea ice in Cape Evans, Antarctica, and provided proof of the potential of using UHI systems for mapping the ice sub-surface. Because of the novelty of the method, more effort is required for UHI systems to become a common method within sea ice research.

4.8 REFERENCES

Alou-Font E *et al.* (2013) 'Snow cover affects ice algal pigment composition in the coastal Arctic Ocean during spring', *Marine Ecology Progress Series*, 474, pp. 89–104.

Arrigo, K.R. (2014) 'Sea Ice Ecosystems', *Annual Review of Marine Science*, 6(1), pp. 439–467. Available at: https://doi.org/10.1146/annurev-marine-010213-135103.

Arrigo, K.R. (2017) 'Sea ice as a habitat for primary producers', *Sea ice*, pp. 352–369.

Babin, M. *et al.* (2003) 'Variations in the light absorption coefficients of phytoplankton, nonalgal particles, and dissolved organic matter in coastal waters around Europe', *Journal of Geophysical Research: Oceans*, 108(C7). Available at: https://doi.org/10.1029/2001JC000882.

Box, J. *et al.* (2012) 'Greenland ice sheet albedo feedback: thermodynamics and atmospheric drivers', *The Cryosphere*, 6(4), pp. 821–839.

Campbell, K. *et al.* (2015) 'Characterizing the sea ice algae chlorophyll a–snow depth relationship over Arctic spring melt using transmitted irradiance', *Journal of Marine Systems*, 147, pp. 76–84.

Campbell, K., Matero, I., *et al.* (2022) 'Monitoring a changing Arctic: Recent advancements in the study of sea ice microbial communities', *Ambio*, 51(2), pp. 318–332.

Campbell, K., Lange, B., *et al.* (2022) 'Net heterotrophy in High Arctic first-year and multi-year spring sea ice', *Elem Sci Anth*, 10(1), p. 00040.

Cimoli, E., Meiners, K.M., *et al.* (2017) 'Spatial variability in sea-ice algal biomass: an under-ice remote sensing perspective', *Advances in Polar Science*, 28(4), pp. 268–296.

Cimoli, E., Lucieer, A., *et al.* (2017) 'Towards improved estimates of sea-ice algal biomass: experimental assessment of hyperspectral imaging cameras for under-ice studies', *Annals of Glaciology*, 58(75pt1), pp. 68–77. Available at: https://doi.org/10.1017/aog.2017.6.

Cimoli, E. *et al.* (2019) 'An Under-Ice Hyperspectral and RGB Imaging System to Capture Fine-Scale Biophysical Properties of Sea Ice', *Remote Sensing*, 11(23). Available at: https://doi.org/10.3390/rs11232860.

Cota, G.F. and Horne, E.P.W. (1989) 'Physical control of arctic ice algal production', *Marine Ecology Progress Series*, 52(2), pp. 111–121.

Ehn, J.K., Mundy, C. and Barber, D.G. (2008) 'Bio-optical and structural properties inferred from irradiance measurements within the bottommost layers in an Arctic landfast sea ice cover', *Journal of Geophysical Research: Oceans*, 113(C3).

Forrest, A.L. *et al.* (2019) 'Exploring Spatial Heterogeneity of Antarctic Sea Ice Algae Using an Autonomous Underwater Vehicle Mounted Irradiance Sensor', *Frontiers in Earth Science*, 7. Available at: https://www.frontiersin.org/article/10.3389/feart.2019.00169 (Accessed: 11 April 2022).

Galindo, V. *et al.* (2017) 'Pigment composition and photoprotection of Arctic sea ice algae during spring', *Marine Ecology Progress Series*, 585, pp. 49–69.

Golden, K., Ackley, S. and Lytle, V. (1998) 'The percolation phase transition in sea ice', *Science*, 282(5397), pp. 2238–2241.

Gosselin, M. *et al.* (1986) 'Physical control of the horizontal patchiness of sea-ice microalgae', *Mar Ecol Prog Ser*, 29(3), pp. 289–298.

Granskog, M.A. *et al.* (2005) 'Scales of horizontal patchiness in chlorophyll a, chemical and physical properties of landfast sea ice in the Gulf of Finland (Baltic Sea)', *Polar Biology*, 28(4), pp. 276–283.

Haas, C. (2017) 'Sea ice thickness distribution', in *Sea Ice*. John Wiley & Sons, Ltd, pp. 42–64. Available at: https://doi.org/10.1002/9781118778371.ch2.

Horner, R. and Schrader, G. (1982) 'Relative contributions of ice algae, phytoplankton, and benthic microalgae to primary production in nearshore regions of the Beaufort Sea', *Arctic*, pp. 485–503.

Jeffrey, S.W., Wright, S.W. and Zapata, M. (2011) 'Microalgal classes and their signature pigments', in C.A. Llewellyn et al. (eds) *Phytoplankton Pigments: Characterization, Chemotaxonomy and Applications in Oceanography*. Cambridge: Cambridge University Press (Cambridge Environmental Chemistry Series), pp. 3–77. Available at: https://doi.org/10.1017/CBO9780511732263.004.

Johnsen, G. *et al.* (2011) 'In vivo bio-optical properties of phytoplankton pigments', in C.A. Llewellyn et al. (eds) *Phytoplankton Pigments: Characterization, Chemotaxonomy and Applications in Oceanography*. Cambridge: Cambridge University Press (Cambridge Environmental Chemistry Series), pp. 496–537. Available at: https://doi.org/10.1017/CBO9780511732263.019.

Johnsen, G. *et al.* (2016) 'The use of underwater hyperspectral imaging deployed on remotely operated vehicles - methods and applications', *10th IFAC Conference on Control Applications in Marine SystemsCAMS 2016*, 49(23), pp. 476–481. Available at: https://doi.org/10.1016/j.ifacol.2016.10.451.

Juhl, A.R. and Krembs, C. (2010) 'Effects of snow removal and algal photoacclimation on growth and export of ice algae', *Polar Biology*, 33(8), pp. 1057–1065.

Kacimi, S. and Kwok, R. (2022) 'Arctic Snow Depth, Ice Thickness, and Volume From ICESat-2 and CryoSat-2: 2018–2021', *Geophysical Research Letters*, 49(5), p. e2021GL097448. Available at: https://doi.org/10.1029/2021GL097448.

Katlein, C., Nicolaus, M. and Petrich, C. (2014) 'The anisotropic scattering coefficient of sea ice', *Journal of Geophysical Research: Oceans*, 119(2), pp. 842–855. Available at: https://doi.org/10.1002/2013JC009502.

Kuczynska, P., Jemiola-Rzeminska, M. and Strzalka, K. (2015) 'Photosynthetic Pigments in Diatoms', *Marine drugs*, 13(9), pp. 5847–5881. Available at: https://doi.org/10.3390/md13095847.

Lange, B.A., Katlein, C., *et al.* (2017) 'Characterizing Spatial Variability of Ice Algal Chlorophyll a and Net Primary Production between Sea Ice Habitats Using Horizontal Profiling Platforms', *Frontiers in Marine Science*, 4. Available at: https://www.frontiersin.org/article/10.3389/fmars.2017.00349.

Lange, B.A., Flores, H., *et al.* (2017) 'Pan-Arctic sea ice-algal chl a biomass and suitable habitat are largely underestimated for multiyear ice', *Global Change Biology*, 23(11), pp. 4581–4597. Available at: https://doi.org/10.1111/gcb.13742.

Lange, B.A. *et al.* (2019) 'Contrasting Ice Algae and Snow-Dependent Irradiance Relationships Between First-Year and Multiyear Sea Ice', *Geophysical Research Letters*, 46(19), pp. 10834–10843. Available at: https://doi.org/10.1029/2019GL082873.

Lavoie, D., Denman, K. and Michel, C. (2005) 'Modeling ice algal growth and decline in a seasonally ice-covered region of the Arctic (Resolute Passage, Canadian Archipelago)', *Journal of Geophysical Research: Oceans*, 110(C11). Available at: https://doi.org/10.1029/2005JC002922.

Legendre, L. and Gosselin, M. (1991) 'In situ spectroradiometric estimation of microalgal biomass in first-year sea ice', *Polar Biology*, 11(2), pp. 113–115. Available at: https://doi.org/10.1007/BF00234273.

Leu, E. *et al.* (2015) 'Arctic spring awakening – Steering principles behind the phenology of vernal ice algal blooms', *Progress in Oceanography*, 139, pp. 151–170. Available at: https://doi.org/10.1016/j.pocean.2015.07.012.

Liang, Y. *et al.* (2022) 'Contribution of warm and moist atmospheric flow to a record minimum July sea ice extent of the Arctic in 2020', *The Cryosphere*, 16(3), pp. 1107–1123. Available at: https://doi.org/10.5194/tc-16-1107-2022.

Light, B., Maykut, G.A. and Grenfell, T.C. (2004) 'A temperature-dependent, structural-optical model of first-year sea ice', *Journal of Geophysical Research: Oceans*, 109(C6). Available at: https://doi.org/10.1029/2003JC002164.

Lorenzen, C.J. (1967) 'Determination of chlorophyll and pheo-pigments: spectrophotometric equations', *Limnol. Oceanogr.*, 12, pp. 343–346.

Lund-Hansen, L.C. *et al.* (2014) 'Removal of snow cover inhibits spring growth of Arctic ice algae through physiological and behavioral effects', *Polar Biology*, 37(4), pp. 471–481. Available at: https://doi.org/10.1007/s00300-013-1444-z.

Lund-Hansen, L.C. *et al.* (2017) 'Is colonization of sea ice by diatoms facilitated by increased surface roughness in growing ice crystals?', *Polar Biology*, 40(3), pp. 593–602. Available at: https://doi.org/10.1007/s00300-016-1981-3.

Lund-Hansen LC *et al.* (2020) 'Effects of increased irradiance on biomass, photobiology, nutritional quality, and pigment composition of Arctic sea ice algae', *Marine Ecology Progress Series*, 648, pp. 95–110.

Lund-Hansen, L.C. *et al.* (2020) 'Spring, Summer and Melting Sea Ice', in L.C. Lund-Hansen et al. (eds) *Arctic Sea Ice Ecology: Seasonal Dynamics in Algal and Bacterial Productivity*. Cham: Springer International Publishing, pp. 61–101. Available at: https://doi.org/10.1007/978-3-030-37472-3_4.

Marzano, F.S. (2014) 'Radiative Transfer, Theory', in E.G. Njoku (ed.) *Encyclopedia of Remote Sensing*. New York, NY: Springer New York, pp. 624–634. Available at: https://doi.org/10.1007/978-0-387-36699-9_152.

Meiners, K.M. *et al.* (2012) 'Chlorophyll a in Antarctic sea ice from historical ice core data', *Geophysical Research Letters*, 39(21). Available at: https://doi.org/10.1029/2012GL053478.

Meiners, K.M. *et al.* (2017) 'Antarctic pack ice algal distribution: Floe-scale spatial variability and predictability from physical parameters', *Geophysical Research Letters*, 44(14), pp. 7382–7390. Available at: https://doi.org/10.1002/2017GL074346.

Meiners, K.M. and Michel, C. (2017) 'Dynamics of nutrients, dissolved organic matter and exopolymers in sea ice', *Sea ice*, 3, pp. 415–432.

Meredith, M. *et al.* (2019) 'Polar regions'.

Mogstad, A.A., Johnsen, G. and Ludvigsen, M. (2019) 'Shallow-water habitat mapping using underwater hyperspectral imaging from an unmanned surface vehicle: A pilot study', *Remote Sensing*, 11(6), p. 685.

Moisan, T.A. *et al.* (2017) 'Satellite Observations of Phytoplankton Functional Type Spatial Distributions, Phenology, Diversity, and Ecotones', *Frontiers in Marine Science*, 4. Available at: https://www.frontiersin.org/article/10.3389/fmars.2017.00189.

Mundy, C. *et al.* (2007) 'Linking ice structure and microscale variability of algal biomass in Arctic first-year sea ice using an in situ photographic technique', *Polar Biology*, 30(9), pp. 1099–1114.

Mundy, C.J. *et al.* (2007) 'Influence of snow cover and algae on the spectral dependence of transmitted irradiance through Arctic landfast first-year sea ice', *Journal of Geophysical Research: Oceans*, 112(C3). Available at: https://doi.org/10.1029/2006JC003683.

Naumann, A.K. *et al.* (2012) 'Laboratory study of initial sea-ice growth: properties of grease ice and nilas', *The Cryosphere*, 6(4), pp. 729–741.

Nghiem, S.V. *et al.* (1995) 'Polarimetric signatures of sea ice: 1. Theoretical model', *Journal of Geophysical Research: Oceans*, 100(C7), pp. 13665–13679. Available at: https://doi.org/10.1029/95JC00937.

Parkinson, C.L. and Comiso, J.C. (2013) 'On the 2012 record low Arctic sea ice cover: Combined impact of preconditioning and an August storm', *Geophysical Research Letters*, 40(7), pp. 1356–1361. Available at: https://doi.org/10.1002/grl.50349.

PARSONS, T.R., MAITA, Y. and LALLI, C.M. (1984) '4.3 - Fluorometric Determination of Chlorophylls', in T.R. PARSONS, Y. MAITA, and C.M. LALLI (eds) *A Manual of Chemical & Biological Methods for Seawater Analysis*. Amsterdam: Pergamon, pp. 107–109. Available at: https://doi.org/10.1016/B978-0-08-030287-4.50034-7.

Peng, G. and Meier, W.N. (2018) 'Temporal and regional variability of Arctic sea-ice coverage from satellite data', *Annals of Glaciology*, 59(76pt2), pp. 191–200. Available at: https://doi.org/10.1017/aog.2017.32.

Perovich, D. *et al.* (2002) 'Seasonal evolution of the albedo of multiyear Arctic sea ice', *Journal of Geophysical Research: Oceans*, 107(C10), p. SHE-20.

Perovich, D.K. (2017) 'Sea ice and sunlight', *Sea ice*, pp. 110–137.

Perovich, D.K. and Elder, B.C. (2001) 'Temporal evolution of Arctic sea-ice temperature', *Annals of Glaciology*. 2017/09/14 edn, 33, pp. 207–211. Available at: https://doi.org/10.3189/172756401781818158.

Petrich, C. and Eicken, H. (2017) 'Overview of sea ice growth and properties', *Sea ice*, pp. 1–41.

Ralph, P.J. *et al.* (2007) 'Melting out of sea ice causes greater photosynthetic stress in algae than freezing in1', *Journal of Phycology*, 43(5), pp. 948–956. Available at: https://doi.org/10.1111/j.1529-8817.2007.00382.x.

Weeks, W.F. and Ackley, S.F. (1986) 'The growth, structure, and properties of sea ice', in *The geophysics of sea ice*. Springer, pp. 9–164.

Wongpan, P. *et al.* (2018) 'Estimation of Antarctic Land-Fast Sea Ice Algal Biomass and Snow Thickness From Under-Ice Radiance Spectra in Two Contrasting Areas', *Journal of Geophysical Research: Oceans*, 123(3), pp. 1907–1923. Available at: https://doi.org/10.1002/2017JC013711.

Wongpan, P. *et al.* (2020) 'Using under-ice hyperspectral transmittance to determine land-fast sea-ice algal biomass in Saroma-ko Lagoon, Hokkaido, Japan', *Annals of Glaciology*. 2020/09/24 edn, 61(83), pp. 454–463. Available at: https://doi.org/10.1017/aog.2020.69.

Yoshida, K. *et al.* (2021) 'Low Fe availability for photosynthesis of sea-ice algae: ex situ incubation of the ice diatom Fragilariopsis cylindrus in low-Fe sea ice using an ice tank', *Frontiers in Marine Science*, 8, p. 221.

5. CHAPTER 3: USE OF UNDERWATER HYPERSPECTRAL IMAGERS (UHI) FOR ASSESSMENT OF SEA ICE ALGAL BIOMASS

This paper has been prepared to be submitted for peer review in the *Journal of Geophysical Research: Oceans*. It represents a core chapter of my thesis and this work was all conducted, analyzed and reported by me as the first author.

5.1 ABSTRACT

Sea ice algae are a key component in the Arctic food web. They remain under sampled due to the limitations of current sampling techniques and the logistical challenges of conducting research in remote polar areas. This study provides an assessment of the use of state-of-the-art remote sensing technologies by remotely estimating sea ice algal biomass using an underwater hyperspectral imager (UHI) in both laboratory conditions and *in situ* in two Svalbard fjords. Normalised difference indices were applied to the UHI surveys and optimal NDI wavelength combinations were obtained for Svalbard surveys and all experimental cultures separately. The NDIs were built based on both standardized radiance and transmittance, the latter exhibiting the best performance for estimating spatial variability of chl *a* biomass. The best performing NDI for the Svalbard surveys were 642:656 nm for standardized radiance and 650:664 nm for transmittance, which explained 98 % and 97 % respectively. The NDI obtained for the best performing experimental culture (639:657 nm and 630:656 nm for standardized radiance and transmittance, respectively), a mixed community from Van Mijenfjorden in Svalbard, was successfully applied to the Svalbard surveys.

5.2 INTRODUCTION

Sea ice algae are an important component in the Arctic marine food web, where their estimated contribution to total primary production in ice-covered ocean areas lies between 3-25 % (Legendre *et al.*, 1992) up to 50-60 % (Fernández-Méndez *et al.*, 2015; Kohlbach *et al.*, 2016).

They provide an important source of food for higher tropic levels in polar ocean, particularly due to their high lipid content (Leu *et al.*, 2015; Kohlbach *et al.*, 2017). Together with other microbial life, like bacteria, algal production in sea ice also influences the biogeochemical cycling of carbon and other elements in the polar oceans (Vancoppenolle *et al.*, 2013; Moreau *et al.*, 2016).

Due to rapid changes to Arctic sea ice cover, including younger and thinner ice as well as earlier retreat, there have been increases in open ocean primary production in parts of the Arctic (i.e. phytoplankton) since 1998 (Arrigo and van Dijken, 2015). However, here is more uncertainty surrounding the response of ice-associated or sympagic production in a warming Arctic, largely attributed to the regional variability of e.g. dominating age of the ice or nutrient regimes (Lannuzel *et al.*, 2020). It has been suggested that ice algal production has the potential to increase in many regions of the Arctic (Lannuzel *et al.*, 2020), largely due to the increased transmission and thus availability of photosynthetically active radiation (PAR) at the bottom of sea ice with a thinner ice cover (Nicolaus *et al.*, 2012). Although increased availability of light favors higher primary production, other factors such as algal photoinhibition with greater exposure to light (Lund-Hansen LC *et al.*, 2020), enhanced nutrient limitation due to enhanced stratification of the water column (Lannuzel *et al.*, 2020) and a shorter overall annual duration of first-year sea ice cover (Post, 2017) have the potential to limit production and counteract such increases in light availability. For example, widespread freshening of surface waters in the Arctic Ocean have already led to an observed decline in nutrients, which is primarily driven by the effects of sea ice loss, such as stronger upper ocean stratification and depletion of nutrient reservoirs because of increased pelagic primary production (Zhuang *et al.*, 2021).

High horizontal patchiness of algal biomass has been observed on multiple scales, from millimeter scale across the skeletal layer (Lund-Hansen *et al.*, 2017) to variability at the meter to kilometer scale due to different sea ice types and the distribution of snow on the surface (Lange *et al.*, 2016; Cimoli, Meiners, *et al.*, 2017; Meiners *et al.*, 2017). The difficulty of characterising this uneven distribution of algae is further compounded by the logistical challenges of sampling in remote locations of the Arctic. Airborne remote sensing of ocean colour is widely used in the monitoring of pelagic blooms in the Arctic (e.g. Neukermans *et al.*, 2018; Zhang *et al.*, 2018) and around the world. However, measurements of sea ice algal production are generally restricted to localised sampling sites, as the presence of ice cover prevents the use of airborne remote sensing. Commonly used methods like ice coring are destructive, time consuming, and only provide information from one point location. In turn this

can potentially lead to a bias when estimates of larger scale spatio-temporal variability of ice algal biomass and production are sought after (Miller *et al.*, 2015; Cimoli, Meiners, *et al.*, 2017; Lange *et al.*, 2017).

Recent advances for remotely estimating ice algal biomass have been made using under-ice irradiance measurements (Mundy *et al.*, 2007; Cimoli, Meiners, *et al.*, 2017; Lange, Katlein, *et al.*, 2017; Campbell *et al.*, 2022). In these methods, the spectral distribution of light transmitted through sea ice, which is altered by the wavelength-specific absorption of ice algal pigments, is related to the physically sampled concentration of ice algal chlorophyll *a* (chl *a*) (Perovich *et al.*, 1993; Mundy *et al.*, 2007). The spectra within this linear relationship between light and chl *a* may be characterised using a spectral transmission ratio of two wavelengths T671:T540 nm (Legendre and Gosselin, 1991) a Normalized difference index (NDIs) of transmitted irradiance (Mundy et al., 2007: Campbell et al. 2015) or transmittance (Campbell et al., 2021), or ben model list here (Mundy *et al.*, 2007; Campbell *et al.*, 2015). Following the determination of specific relationship between light and physically sampled chl *a* have been established, NDIs light measured from an upwards facing spectral sensor can solely be used to estimate ice algal chl a over larger spatiotemproal scales. The use of NDIs has become particularly widespread in both the Arctic and Antarctic, although the specific combination of wavelengths has varied due to regional differences in non-algal absorbing particles within the ice and the variability of the concentration of accessory pigments (Campbell *et al.*, 2015, 2022; Melbourne-Thomas *et al.*, 2015). While these methodological advancements have drastically improved our ability to assess the spatiotemporal variability of ice algal blooms in a time of rapid environmental change, one outstanding limitation is their integration of spectral absorption over the effective foot print of the sensor, typically around 1,5-2 m, depending on how close to the sea ice subsurface the sensor is. As a result, they cannot take into account smaller scale (i.e. mm) variability of biomass known to occur within sea ice algal blooms (Cimoli, Meiners, *et al.*, 2017). Underwater hyperspectral imagers (UHI) have only recently become available in marine research and show great potential to assess this knowledge gap, as they are capable of imaging at the sub-millimeter scale (Cimoli, Lucieer, *et al.*, 2017; Cimoli, Meiners, *et al.*, 2017). Unlike other light sensors with a comparatively wide footprint, hyperspectral imagers collect spectral information with a pixel-scale resolution, capturing variability across multiple scales. Hyperspectral imagers have only recently become available for marine research, and methods for deployment and data processing for UHI systems have not yet been developed.

The aim for this study was to further assess the potential of UHI technology in effectively studying sea ice algal blooms. Specifically, we used an UHI to estimate, for the first time in fjord systems, the distribution of ice algal chl *a* biomass in two Svalbard fjords. These observations are coupled to controlled laboratory experiments on cultured ice algae that investigate the relationship between the under-ice spectral measurements and chl *a* biomasa. From this work we offer new insights on the optimal NDI combination for such coastal systems. We also help to better characterise the variability of ice algae on the sub-millimeter scale for more representative estimates of overall biomass and explain the pigment-related causes of spectral variability when using remote sensing tools to monitor ice algal blooms.

5.3 Materials and Methods

5.3.1 Field

5.3.1.1 Study area and sampling sites

Field sampling took place in the fjords of Tempelfjorden (78.41 °N, 17.08 °) and Van Mijenfjorden (77.80 °N, 15.76 °E) on the west coast of Svalbard. Tempelfjorden is a smaller fjord (14 km long and 5 km wide) that is more directly linked to the coastal Atlantic water (e.g. Nilsen et al., 2008) compared to Van Mijenfjorden (50 km long and 10 km wide), which is characterised by the island Akseløya at the mouth of the fjord that limits Atlantic inflow. The environmental conditions at Tempelfjorden are also more influenced by glacial freshwater inputs from Tunabreen (e.g. Fransson et al., 2015) .Three sampling sites were studies, one in Tempelfjorden (TF1), and two in Van Mijenfjorden (VM1 and VM2;fig. 1).

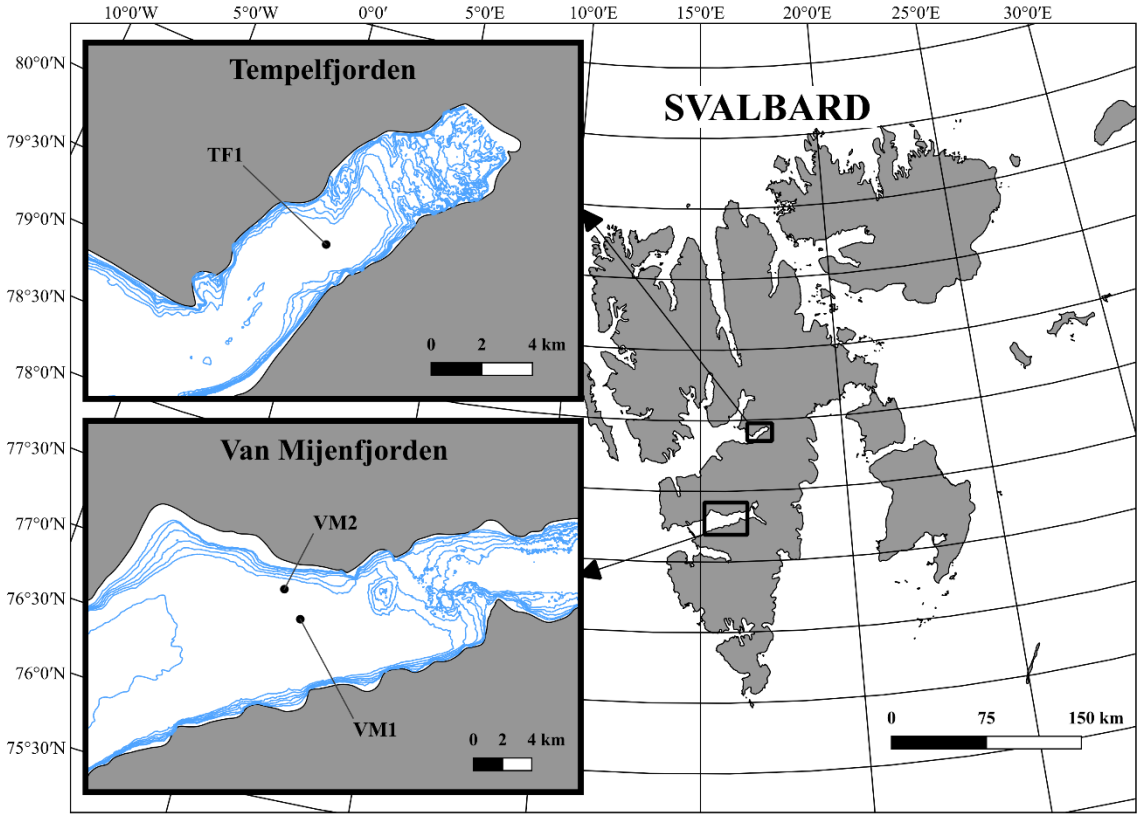

Figure 1. Map of the sampling sites TF1 (78.41 °N, 17.08 °), VM1 (77.80 °N, 15.76 °E) and VM2 (77.82 °N, 15.71 °E) in Tempelfjorden and Van Mijenfjorden in Svalbard.

5.3.1.2 HYPERSPECTRAL IMAGING AND SAMPLING

Under-ice hyperspectral surveys were conducted using a UHI (Ecotone AS, Trondheim, Norway, Model 4) with a manufacturer radiometric calibration. The UHI was attached to an under-ice arm (**Fig 2 a,b**.) which allowed the positioning of the UHI in an upwards facing manner immediately below the subsurface of the ice, at a horizontal distance of 1.1 m from the deployment hole. The UHI was positioned to face the direction of the sun in an effort to minimize the influence of the light coming from the deployment hole. The UHI sampling events at a given site consisted of six consecutive surveys in a C-shape (180 °) around the deployment hole, which resulted in a sub-ice areal coverage of approximately 1.0 x 0.5 m (968 x ~ 2000 pixels), where each pixel collected spectral radiance in 214 wavelength bins. Due to the limited movement with the arm, the survey was completed in 6 sections, ranging from a-f and. After collecting 3-4 ice cores, an additional UHI survey (from here on control scan) was performed for the cored area (sections C and D) for the validation of the chl *a* concentration and the under-

ice spectra from the cored area. This was done to ensure that the spectra for assessing the relationship between under-ice spectra and measured chl *a* could be extracted from the exact sampled area.

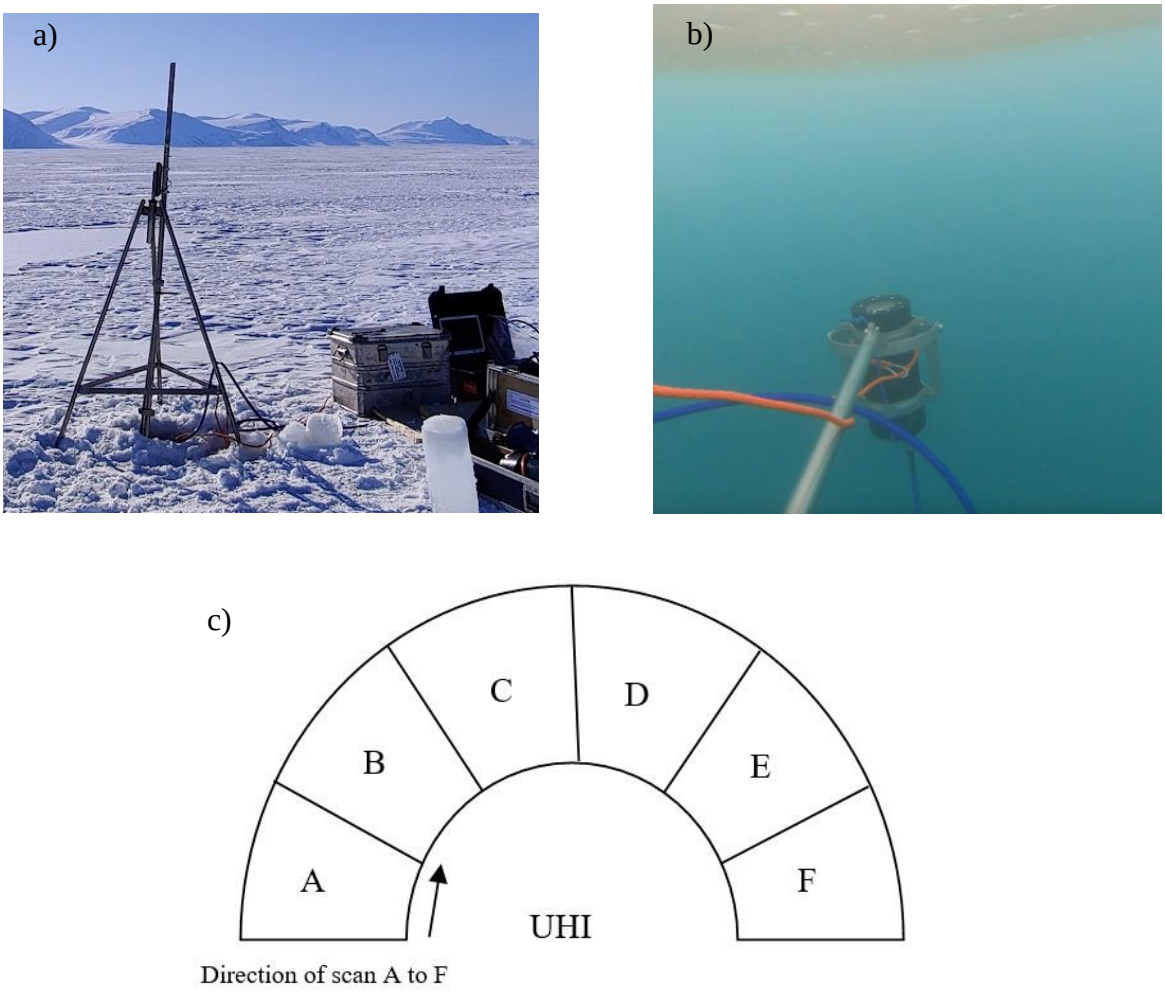

Figure 2. Overview of the setup for sub-ice UHI measurements. a) Picture of the under-ice arm from above the ice when the UHI is deployed, b) The UHI attached to the under-ice arm which pivots the UHI to an upwards looking position under the ice, and c) Schematic of the UHI-survey sections a-f around the UHI.

5.3.1.3 BIOLOGICAL MEASUREMENTS

Ice cores (n = 4) were collected for assessment of chl *a* using a 9 cm ice corer (Kovacs Enterprise Mark II) following each of the UHI surveys. Each core was taken at a distance of 30 cm from one another (REF figure in 2.1.2), and the bottom 3 cm from each were melted individually with filtered seawater (FSW) to buffer for changes in salinity. Following approximately of 24h of melt the melted ice cores were filtered onto 25-mm GF/F filters (Whatman), which were then placed in 90 % acetone for 18-24 h for pigment extraction. The average chl *a* was determined before and after acidification using a fluorometer (Turner Designs Trilogy Fluorometer; Parsons et al., 1984). Pigments were detected with a Waters Alliance 2695 HPLC Separation Module connected to a Waters photodiode array detector (2,996). The solvents were HPLC-grade (Merck) and for the peak separation an Agilent Technologies Microsorb-MV3 C8 column (4.6 x100 mm) was used. The auto sampler module was set to 4 °C during the entire measurement. In total 200 µl sample were injected with an auto addition function of the system between sample and a 1 molar ammonium acetate solution in the ratio of 60:40:60:40. Peaks were identified and quantified with the EMPOWER software. More details about sample preparation, solvents and gradients can be found in Tran et al., 2013.

5.3.2 LABORATORY EXPERIMENT

The experimental setup consisted of six acrylic tanks (30 cm x 30 cm x 30 cm) that were matte black on side walls to minimise reflection of light and optically clear on the bottom to permit UHI imaging from below (**Fig 3).** The acrylic tanks were illuminated using Namron LED RBG + W lights, installed in a downward facing direction above the biofilm tanks. Diffuser plates were also installed between the LEDs and tanks to ensure an even distribution of light. The intensity of the lights were adjusted until light intensities ranging between 26-33 µmols photons m^{-2} s^{-1}, which corresponded to the growth light intensity of stock cultures.

5.3.2.1 ALGAL CULTURING

A total of three algal cultures were grown for experimentation in this study: i) mix of *Attheya sp.* And unidentified flagellate (ATT), ii) monoculture of *Eucampia groenlandica* (EUC), and

iii) a mixed community from Van Mijenfjorden in Svalbard (VMC) that was collected from VM2 during fieldwork (Section 2.1.1). The species composition of VMC was dominated by pennate diatoms at the time of the experimentation (Forgereau et al. 2022, *in prep*). These cultured algae were grown in Artificial Sea Water (ASW) following the protocol of the American Society for Testing and Materials (ASTM D1141-98) and Guilliard F/2 media (Guillard and Ryther, 1962) with a salinity of approximately 35. Prior to experimentation, the cultures were grown at 4 °C (INCU-Line 150R Premium incubator) at a light intensity of 30 µmol photons m^{-2} s^{-1} for approximately four months prior to upscaling. In the first phase of upscaling, 10 % of culture stock was added into 5 corning culture flasks per containing 50 ml of F2 + ASW. This was done for each culture separately. The second phase of upscaling took place 10 days later, where the contents of the culture flasks were transferred into 3 x 1900 ml of autoclaved F2+ ASW.

During exponential phase of growth of each algal culture (**Supplementary Fig. 2**) was transferred to the biofilm tanks, while using care to prevent cross contamination of strains. The growth rate of ATT, EUC and VMC were 0.18, 0.01 and 0.35, respectively. Each culture was grown in two adjacent tanks, one for sampling purposes and the other was left undisturbed for imaging only (**Fig. 3b**). Nutrient levels were monitored and 20 % of media was replaced regularly at a weekly interval. From here, on the cultures were grown as a dense layer covering the bottom of the tanks that is hereafter referred to as a biofilm.

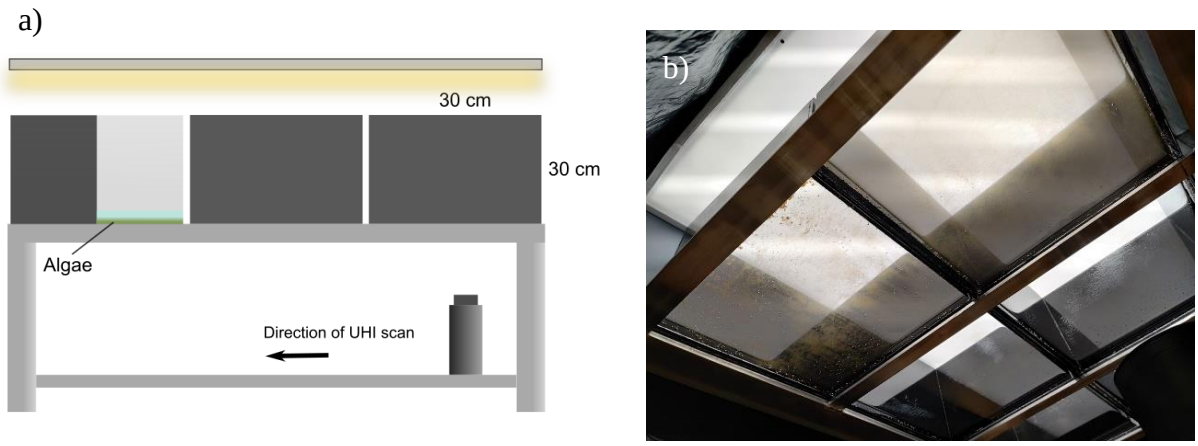

Figure 3. Setup of biofilm imaging tanks. a) illustration of biofilm tanks and UHI surveying setup b) picture of the clear-bottomed biofilm tanks from below showing VMC in the front.

5.3.2.2 HYPERSPECTRAL IMAGING AND SAMPLING

The UHI was mounted in an upward looking position on a motorized stand that moved on a rail horizontally across the table in a total of 9 transects. To capture the entire tank subsurface, three transects were chosen per tank, two on the sides and one in the middle. Each UHI survey consisted of approximately 500x800 pixels, each pixel consisting of 369 spectral wavelength bins. Each line had an integration time of 40 µS and exposure was set to 40.

Similar to the *in situ* surveys (Section 5.3.1.2), an additional control scan was performed after sampling for locating the exact location of the sampled areas for extracting the spectra. All surveys were performed in the dark to exclude the influence of any other light sources. The first survey was conducted two days after transferring the cultures to the tanks to allow settling of the algae to the bottom of the tank. Surveys were then conducted every 3rd day for a total of six (ATT and VMC) to 8 weeks (EUC). These intervals were chosen to ensure that each survey represented a different level of biomass.

Samples of chl *a* and pigments for HPLC (High Performance Liquid Chromatography) were collected after each complete UHI survey for the validation of the under-tank spectra and biomass relationship. Sample locations were chosen at random, but areas with clear aggregates were avoided, especially for ATT. A watertight cylinder with a diameter of 5 cm was used to ensure sample collection of a controlled area and volume. The sample was sucked into a syringe while simultaneously scraping the area within the cylinder. Both chl *a* and HPLC samples were immediately filtered onto Whatman GF/F filters. Samples for Chl *a* samples were extracted in 90 % acetone for 18-24 hours and measured for chlorophyll *a* content using a Turner Designs Trilogy fluorometer (Parsons et al., 1984). HPLC samples were folded in aluminium foil and stored in -80 °C until analysis at the Alfred Wegener institute 4 months later (see section 2.1.3 for a detailed description of the method).

5.3.3 DATA PROCESSING AND ANALYSIS

Pre-processing of all hyperspectral images and extraction of spectral information were done using Python (version 3.8.8.). The ice core (Svalbard) and sample areas (experiment) were located manually using the control scan in QGIS (version 3.22.7) to guarantee the extraction of

spectra from the exact area sampled. The control scan was overlaid over the initial scan using visible features to find the best fit of the two scans. The spectra were then extracted from the cored area, covering around 80 % of the area of the core to avoid bias due to potential sample loss at the edges caused by coring.

The radiance data was processed through two different approaches: i). by standardizing (centering the mean) all collected spectra from the sampled area to investigate the differences in the spectral profile instead of magnitude, and ii) by dividing the spectra from an area with visible algae with a clear, sampled area (experiment) or the core hole after coring (Svalbard), in order to calculate transmittance. Standardizing the radiance by centering the mean allows for easier comparison by excluding differences in the magnitude of the light.

This was done to compare different approaches for which approach gives the most reliable estimate of chl *a*.

Normalized difference indices (NDI) were calculated according to the following equation:

$$NDI = [T(\lambda 1) - T(\lambda 2)] / [T(\lambda 1) + T(\lambda 2)],$$

where T(λx) represent transmittance at a given wavelength. Calculations were performed on wavelengths within the range of 381-750 nm to capture the variability within the range of photosynthetically active radiation 400-700 nm (from here on PAR). Following Mundy et al (2007) and Campbell et al (2014), Pearson correlation surfaces were constructed to examine all possible NDI wavelength combinations and the correlation with measured chlorophyll *a* concentration for both standardized irradiance and transmittance. Optimal NDIs were chosen based on three main criteria 1) correlation factor 2) within first absorption peak of chl *a*, 3) preference towards wavelength combinations below 570 nm to avoid influence of snow. A distance of a minimum 5 nm between the two chosen wavelengths was kept to avoid artificial correlation between neighbouring wavelengths. Optimal NDIs were obtained through correlation surfaces for all experimental cultures separately and combined as well as all field surveys pooled together. Two NDI combinations were calculated for each, based on standardized irradiance and transmittance, to investigate which approach performed better.

Since only 3-4 samples for the validation of under-ice spectra to chl *a* were collected at each Svalbard site, all sites are combined to increase the robustness of the statistical analyses.

Correlation matrices for all possible NDI wavelength combinations and snow thickness were also constructed investigate the effect of snow on the spectral signature in this region.

5.4 RESULTS AND DISCUSSION

5.4.1 ENVIRONMENTAL AND BIOLOGICAL CHARACTERISTICS – SVALBARD

Environmental conditions, such as sea ice thickness and snow depth, and biological parameters are summarized in **Table 1**. Snow and ice thickness varied across all sites, with the thickest snow (12.5 ± 2 cm) at VM1 and thickest ice at VM2(40.71 ± 1.27 cm) measured at VM1. The thinnest snow was measured at VM2 (3 ± 0) and thinnest ice at TF1 (31.6 ± 0.47). Lowest integrated PAR was measured at VM1 (0.42 ± 0.08) and highest at TF1 (2.82 ± 0.09). Average core-derived chl *a* concentrations per site are summarized in **Table 1.** The lowest chl *a* concentrations were measured at TF1 (0.39 ± 0.13 mg/m^{-2}), while substantially higher concentrations were measured at VM1 (6.58 ± 0.71 mg/m^{-2}). The species composition at all sites were dominated by pennate diatoms, with an average proportion of 97.5 % at VM1 and VM2, and a proportion of 66 % at TF1 where the remaining 34 % mostly composed of different flagellates (Forgereau et al., *in prep*).

Table 1. Physical and biological characteristics of all sampling sites.

Site	TF1	VM1	VM2
Date	April 12th	April 17th	April 14th
Coordinates	78.41 °N, 17.08 °	77.80 °N, 15.76 °E	77.82 °N, 15.71 °E
Snow depth (cm)	7.5 ± 0.4	3 ± 0	12.5 ± 2
Ice thickness (cm)	31.6 ± 0.47	57± 0	40.71 ± 1.27
Average PAR (µmols photons m^{-2} s^{-1})	2.82±0.09	0.42±0.08	1.35±0.16
Chlorophyll *a* (mg/m^{-2})	0.39 ± 0.13	0.78 ± 0.22	6.58 ± 0.71

5.4.2 EXPERIMENTAL CULTURES

The experimental cultures exhibited different growth rates (**Supplementary Fig. 2**) and distributions of chl *a* biomass (**Supplementary Fig. 1**) across the biofilm tank subsurface

during experimental periods. The ATT culture rapidly formed a dense layer at the bottom of the tank within 3 days, but showed no signs of biofilm formation. A biofilm here is referred to layer of algal cells adhered to the surface of the tank via a mucous substance. This led to aggregate formation during chl *a* sampling that likely contributed to fluctuations in chl *a* destructively sampled during experiments (**Supplementary Fig 3**). In comparison, the VMC culture formed an evenly distributed biofilm within 3 days of tank inoculation, and the distribution of biomass was relatively uniform with slight accumulation of biomass in the middle of the tank (**Supplementary Fig 1**). The EUC culture displayed slower growth than the other two cultures (**Supplementary Fig. 3)** which translated to a longer experimental period to include a clear enough increase in biomass (up until ~ 1000 µg/L^{-1}). The culture had an even distribution of chl *a* biomass across the tank (**Supplementary Fig. 1)**.

A baseline measurement of the media without algae was conducted prior to the experiment. The spectra showed a strong peak at around 450 nm (**Fig. 4a**), which is in line with previous studies using white LED lights as a light source (Cimoli, Lucieer, *et al.*, 2017). This served as the baseline spectra when calculating transmittance. To remove this influence from algal absorption signatures during experiments, these spectra of the baseline LED light and growth media in the absence of algae were used to standardise UHI surveys. It follows that all UHI surveys using transmittance presented hereafter have been divided by their baseline spectra without algae (**Fig. 4b**) unless otherwise specified.

As expected, spectra extracted from areas with algal biomass display strong absorption around wavelengths affiliated with chl *a* absorption, around 440nm and 670 nm (**Fig. 4b**), which is especially apparent for ATT.

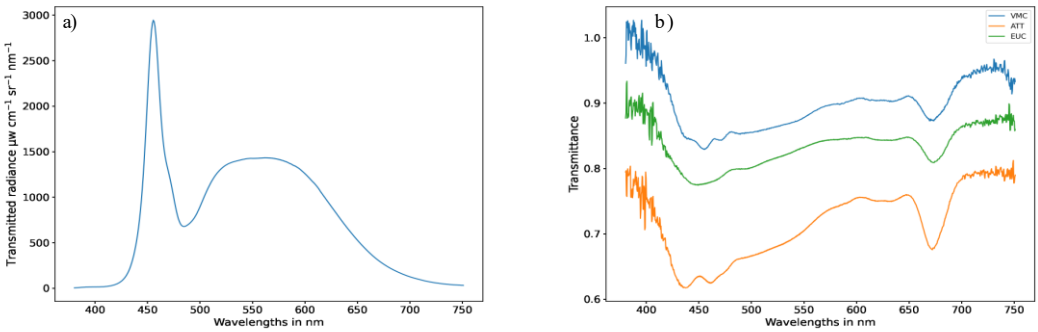

Figure 4. Average spectral radiance of the biofilm tanks measured by the UHI. a) Average raw baseline spectra without algae, recorded prior to each experiment. b) Transmittance of patches of algae from all cultures, representing similar chl *a* biomass levels.

5.4.3 Optimal NDIs

5.4.3.1 Optimal NDIs– Svalbard surveys

Optimal NDI combinations were obtained for all sites combined.

The best performing wavelength pairs for all sites combined were 642:656 nm (R^2=0.98, n= 11) for standardized radiance and 650:664 nm (n=11, R^2=0.97) and for transmittance. They explained 98% and 97% of total variation of algal biomass, respectively (**Fig.X**). Remote estimates of chl *a* (mg/m^{-2}) concentration were calculated using the following linear regression models for (i) standardized radiance and (ii) transmittance:

i. Chl *a* (mg/m^{-2}) = 65.6419289 mg/m^{-2} x $NDI_{650:664}$ -0.96299309 mg/m^{-2}

ii. Chl *a* (mg/m^{-2}) =89.60259354 mg/m^{-2} x $NDI_{642:656}$ -17.70501136 mg/m^{-2}

The resultant chl *a* concentration (mg/m^{-2}) was applied to the UHI survey in VM1 for estimating chl *a* biomass distribution per pixel (0.5 x 0.5 mm) across the survey (**Fig. 5).**

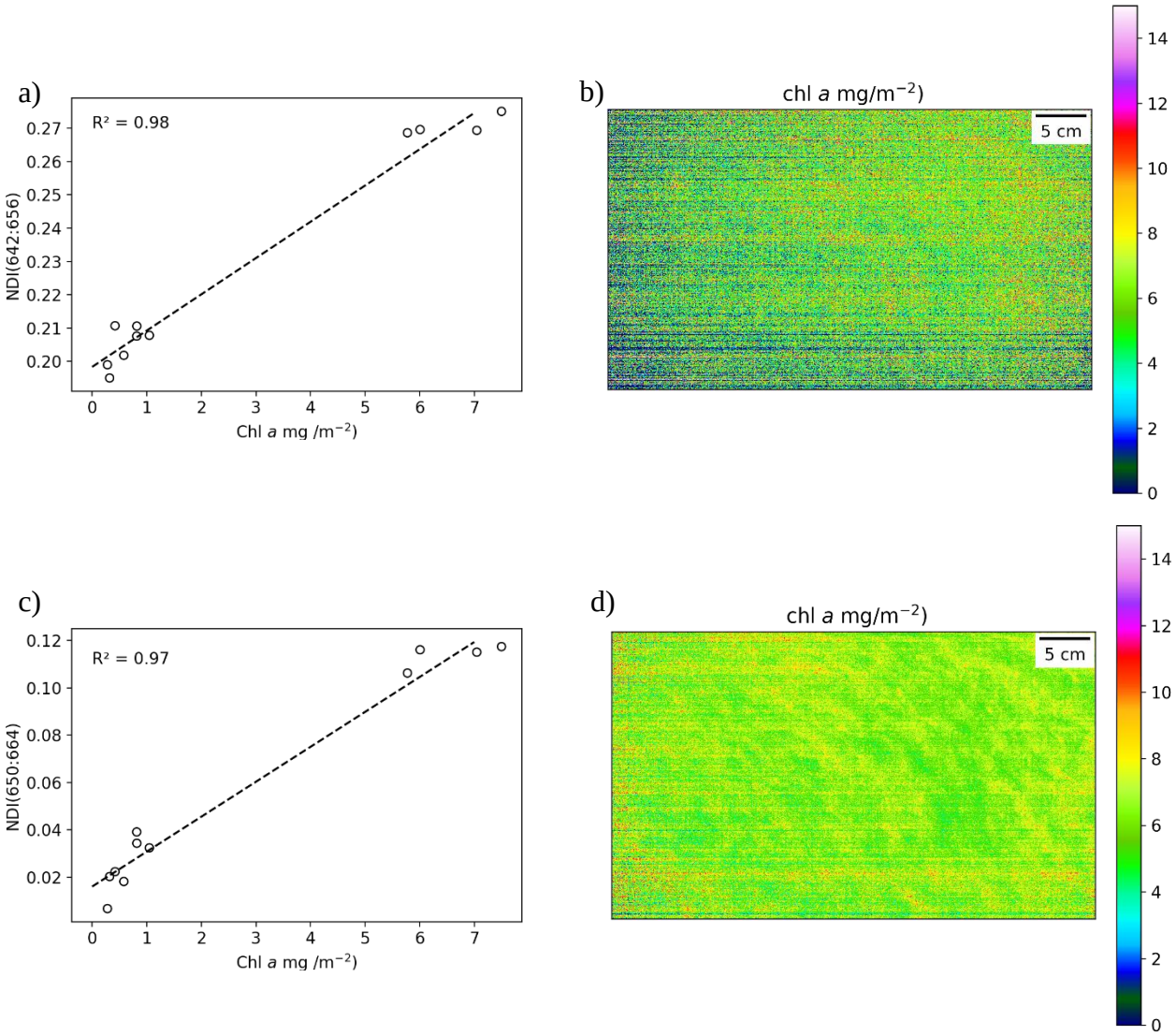

Figure 5. Remote estimates of chl *a* concentration (mg/m^{-2}) at VM1. a) linear regression of measured chl *a* and NDI (642:656 nm, n=11, R^2=0.98) based on standardized radiance, b) chl *a* matrix of estimated chl *a* distribution using NDI (650:664 nm), linear regression of measured chl *a* and NDI (642:656 nm, n=11, R^2=0.97) based on transmittance (%), and d) chl *a* matrix of estimated chl *a* distribution using NDI (650:664 nm).

The chl *a* images capture the distribution and variability of chl *a* on a scale from sub-millimeter to 50 cm scale. In this comparison, the image based on transmittance performed better in displaying the patches of algal distribution (**Fig. 5d**).

Interestingly, the highest correlations were in our study centered around the second chl *a* absorption peak, in contrast to previously reported NDIs (Mundy *et al.*, 2007; Campbell *et al.*, 2014). According to Wongpan et al. (2018), wavelengths around the second absorption peak

are favoured when the snow depth is below 0.1 m, and the snow is thus thin enough that it does not exhibit a significant enough influence on the spectra. Out of the total 11 ice cores samples, only three had snow depths above 0.1 m (average 12.5 cm± 2.06 cm).

There was an apparent correlation between snow depth and chl *a* (r= 0.81, p= 0.002), which is indicated a positive relationship with snow depth and chl *a*, in contrast to previously reported relationships (e.g. Campbell et al., 2015; Mundy et al., 2007). We suspect this is likely in part due to the limited sample size of this study and the relationship is influenced by other factors due to contrasting environmental conditions between the study sites. Nevertheless, correlation surfaces constructed between snow depth and UHI spectra indicated that the highest correlations (r > 0.9) were within wavelengths pairs between 575-608 nm for standardized irradiance and 670-690 nm for transmittance. Such wavelength combinations do not overlap with the optimal NDIs identified for chl *a* prediction. Wavelength pairs for the first absorption peak of chl *a* (440 nm) were also investigated, where the optimal NDI combination for standardized spectra was 473:482 (R^2=0.49, n=11) and transmittance 443:453 (R^2=0.45, n=11). While the optimal NDIs chosen for our model overlap with the range for snow absorption, our NDIs within the red wavelengths showed substantially higher correlations with core-derived chl *a*.

The HPLC analysis indicated relatively high concentrations of the pigment fucoxanthin (145.9 ± 19.6 µg/L^{-1}), compared to other pigments measured (**Fig 6**), which is a widely found pigment in diatoms (Jeffrey, Wright and Zapata, 2011), in all samples from VM1. Much lower concentrations were measured for samples from VM2 (12.8 ± 2.8 µg/L^{-1}) and TF1(10.28 ± 2.3 µg/L^{-1}).

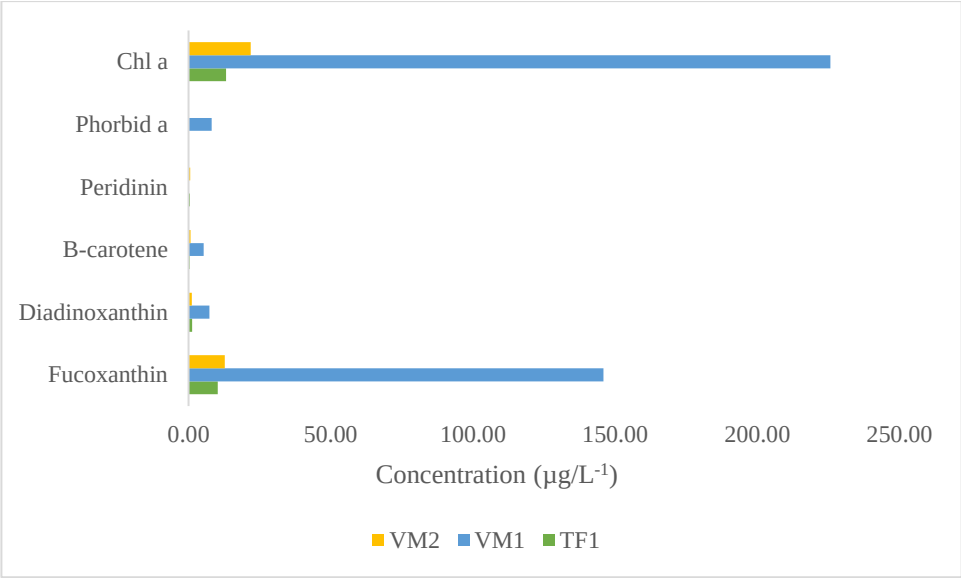

Figure 6. Concentration of accessory pigments (µg/L^{-1}) measured in TF1, VM1 and VM2.

The sea ice algal community at VM1 was diatom dominated, while TF1 displayed a higher proportion of flagellates (Martín et al. *in prep*). The higher concentration of fucoxanthin in VM1 could therefore be attributed to diatoms. Fucoxanthin absorbs wavelengths in the range of 450-540 nm and could therefore have an effect on the results of the correlation matrices, where it may overlap with the absorption of chl *a*. This insight is supported by previous observations that the increased production of accessory pigments, such as fucoxanthin or xanthophylls (e.g., diadinoxanthin), can lead to an underestimation of chl *a* by bio-optical models due to their overlap in absorption spectra (Cimoli, Meiners, *et al.*, 2017).

5.4.3.2 OPTIMAL NDIS – EXPERIMENTAL CULTURES

Table 1. Summary of optimal NDIs for all laboratory cultures with best performing NDIs presented in bold.

	Standardized radiance or transmittance	NDI λ	R^2
VMC (n=10)	Standardized	**639:657**	0.97
	Transmittance	**630:656**	**0.94**
EUC (n=8)	Standardized	419:437	0.89
	Transmittance	665:680	0.86
ATT (n=10)	Standardized	438:671	0.68
	Transmittance	413:650	0.31
COMB (n=28)	Standardized	650:694	0.55
	Transmittance	658:694	0.54
VMC+EUC (n=18)	Standardized	**666:681**	**0.94**
	Transmittance	671:681	0.86

Out of the three experimental cultures, VMC showed the highest correction between sampled chl a and NDI wavelength combinations for standardized radiance and transmittance at 642:656 nm (R^2= 0.98, n=10) and 650:664 (R^2=0.97, n=10), respectively. Similar to the highest correlating wavelengths for SVA, these wavelengths lie on the red absorption peak of chl *a*. EUC displayed the highest correlation for the wavelength pair 419:437 nm (R^2= 0.89) based on standardized radiance and 665:680 nm (R^2=0.85) based on transmittance Correlation surfaces for ATT showed the lowest correlation for any wavelength pairs. It is suspected that the uneven distribution of cells across the biofilm tank affected the spectral measurements, leading to lower correlation for specific wavelengths. The best performing NDI combination was 438:671 nm (R^2= 0.68, n = 10) based on standardized radiance and the optimal NDI for transmittance was 413:650 (R^2=0.31, n=10). Optimal NDIs were also explored for all cultures pooled (COMB) for a more reliable predictor based on a higher sample number. The chosen wavelength pairs were 650:694 nm (R^2= 0.55, n=28) and 658:694 (R^2= 0.54) for standardized and transmittance, respectively. Because of the poorer performance of ATT, we suspect that excluding ATT from COMB could improve the performance of the model, therefore, optimal NDIs were chosen for

a combination of VMC + EUC instead. Removing ATT substantially improved the performance of the pooled model, with optimal NDI combinations of 666:681 nm (R^2= 0.94, n=18) for standardized radiance and 671:681 (R^2=0.86, n=18) for transmittance.

The NDI combinations obtained for VMC exhibited the best performance, chosen as the most representative combination for a natural community, as this community was a subsample of a mixed community from Van Mijenfjorden. A chl *a* matrix for estimating biomass distribution across the tank (**Fig. 7**) was calculated using the following equations, based on linear regression of the optimal NDIs for i) standardized radiance and ii) transmittance, and measured chl *a*:

i. Chl *a* ($\mu g/L^{-1}$) = 65.6419289 $\mu g/L^{-1}$ x $NDI_{660:681}$ -0.96299309 $\mu g/L^{-1}$

ii. Chl *a* ($\mu g/L^{-1}$) =89.60259354 $\mu g/L^{-1}$x $NDI_{667:681}$ -17.70501136 $\mu g/L^{-1}$

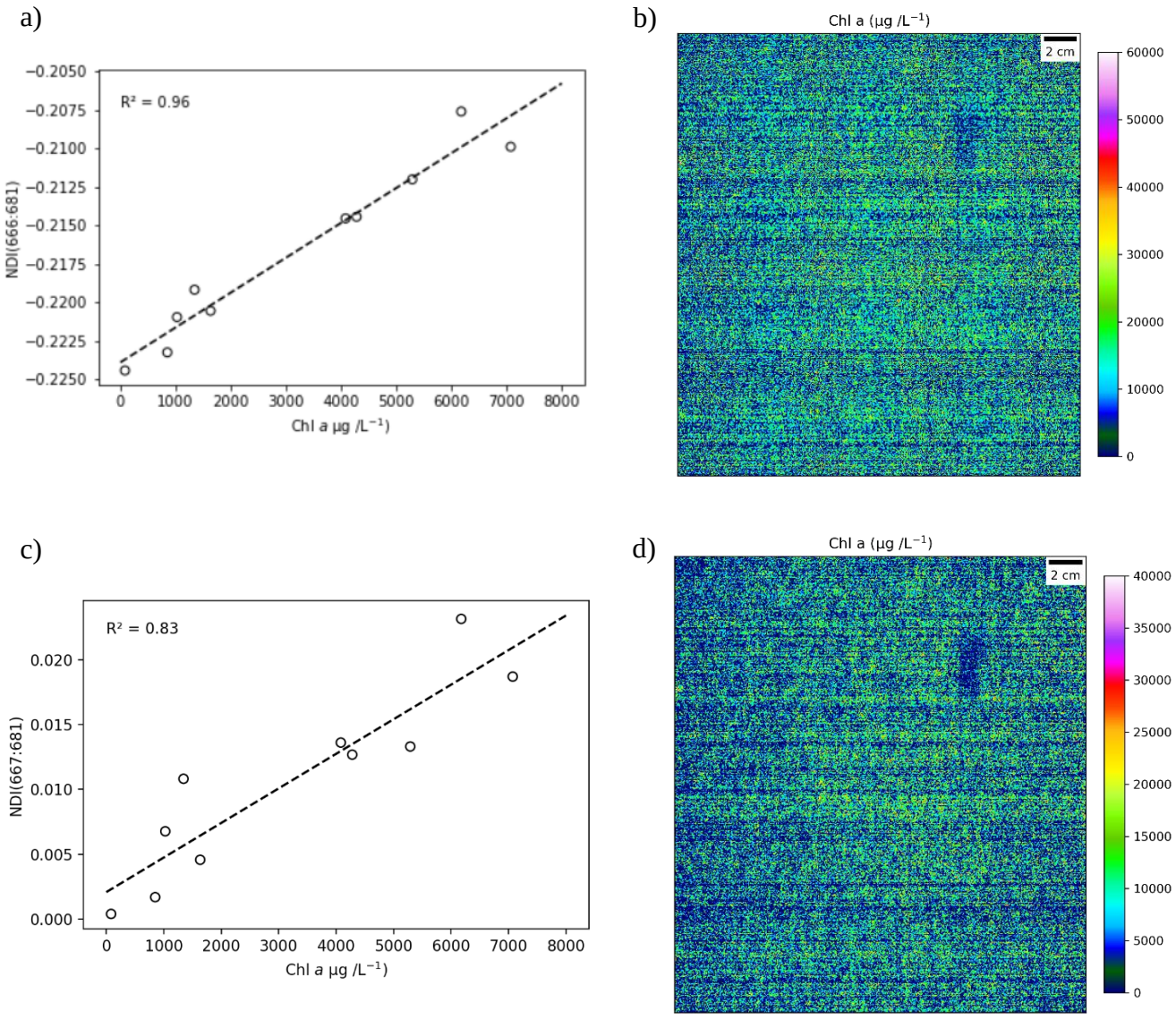

Figure 7. Remote estimates of chl *a* concentration (µg/L-1) for VMC. a) linear regression of measured chl *a* and NDI (666:681 nm, R^2=0.96, n=10) based on standardized radiance, b) chl *a* matrix of estimated chl *a* distribution using NDI (666:681 nm), c) linear regression of measured chl *a* and NDI (667:681 nm, n=11, R^2=0.97) based on transmittance (%), and d) chl *a* matrix of estimated chl *a* distribution using NDI (650:664 nm). Note the differnet scales on the colorbars.

Similar to the Svalbard surveys, the NDI based on standardized spectra (666:681 nm, R^2=0.96, n=10) performed better according to the fit to measured chl *a* concentration. However, the variability of the chl *a* distribution across the biofilm tank is more apparent from the chl *a* image calculated based on transmittance (**Fig. 7d**).

5.4.4 APPLICATION OF EXPERIMENTAL AND REPORTED NDIS

The highest performing NDI combinations obtained from the experimental cultures VMC and VMC + EUC were applied to the Svalbard surveys to investigate the performance of laboratory-based NDIs in natural sea ice. Separate comparisons are presented for NDIs based on standardized radiance and transmittance. An additional comparison was made using two different NDI combinations previously reported by Mundy et al. (2007) and Campbell et al. 2014, both obtained from surveys beneath land-fast FYI and the optimal NDIs in both studies fall within the first absorption peak of chl *a*.

Out of the optimal NDIs of VMC and VMC + EUC based on standardized radiance, VMC 639:657 nm (R^2= 0.95, n=11) performed best when applied to the Svalbard sites. The optimal NDI for VMC + EUC, 666:681 nm (R^2= 0.67, n=11) gave a less reliable estimation of chl *a* compared to VMC.

Similar to the results for the application of standardized radiance NDIs, the best performing NDI model based on transmittance was VMC 630:656 nm (R^2= 0.89, n=11) (**Fig. 8a**)., which explained 89 % of chl *a* biomass variability. Interestingly the NDI for VMC + EUC, 671:681 nm (R^2= 0.02, n=11) performed poorly and only explained 2 % of chl *a* biomass variability **Fig. 8b**). The NDI presented by Mundy et al. 2007, 472:485 nm (R^2= 0.37, n=11), explained only 37 % of biomass variability **Fig. 8c**)., while the NDI combination 478:490 nm (R^2= 0.29, n=11) presented by Campbell et al. (2014) explained (29 % on biomass variance **Fig. 8d**).

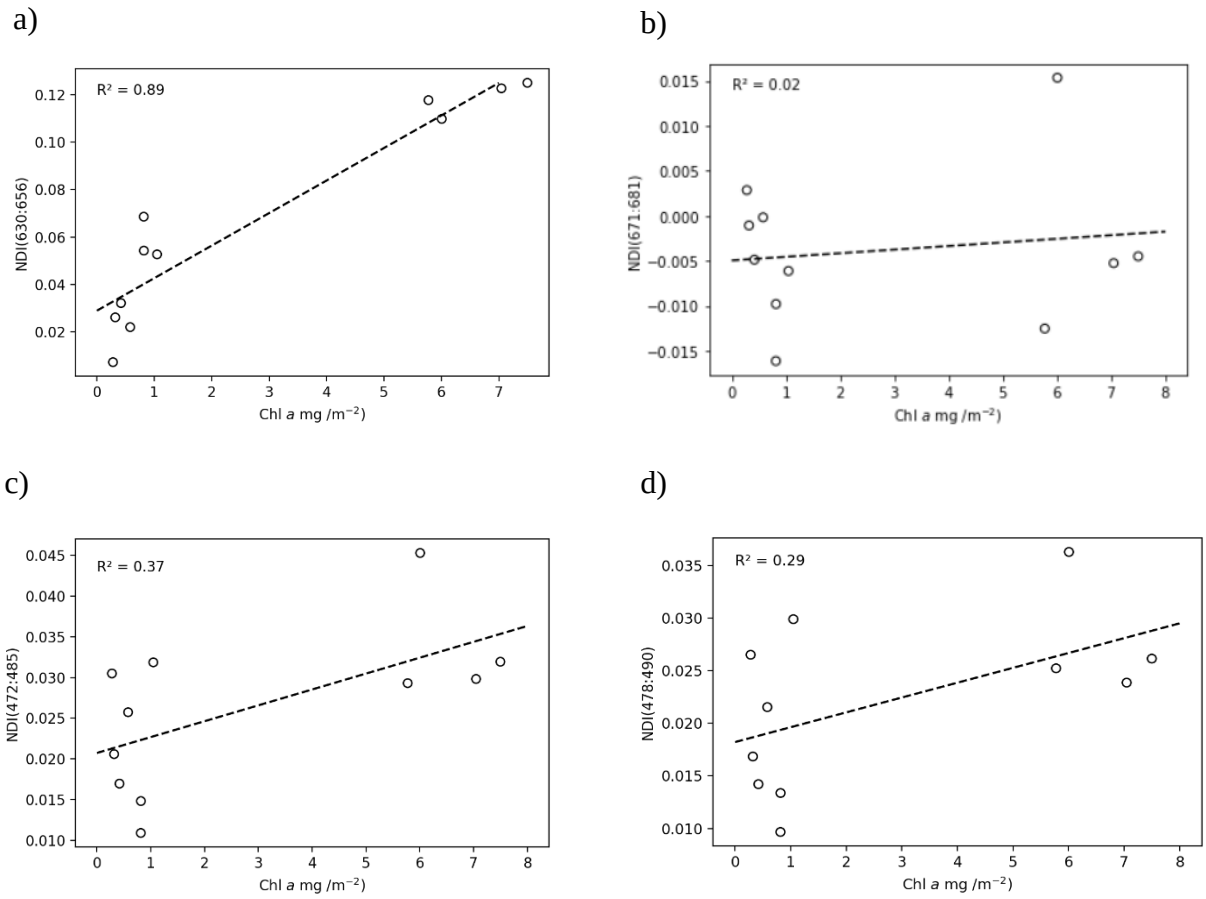

Figure 8. Comparison of linear regressions and R^2 -values for experimental and previously defined NDI combinations applied to Svalbard surveys (transmittance). a) VMC 630:656 nm (R^2= 0.89, n=11), b) VMC + EUC, 671:681 nm (R^2= 0.02, n=11) c) d) Mundy et al. (2007) 472:485 nm (R^2= 0.37, n=11, d) Campbell et al. (2014) NDI 478:490 nm (R^2= 0.29, n=11).

As expected, the VMC NDI displayed the strongest correlation when applied to the Svalbard surveys, while NDIs obtained from other areas of the Arctic did not reliably estimate chl *a* variability for our surveys. The difference in the performance can be attributed to several factors. First and foremost, the VMC community species composition resembles the *in situ* community (Martín et al., *in prep*), which is why the influence on the spectral profile of transmitted light should be similar to that *in situ*. However, the combination of VMC + EUC did not perform well, indicating a different influence on the spectra by species similar to *E. groenlandica.* Applying the NDI combinations obtained in Resolute Passage, Canada, for our Svalbard surveys did not provide reliable estimates of chl *a* biomass variance. In both studies

of Mundy et al. (2007) and Campbell et al. (2014), snow depths were thicker than in our study, which could influence the performance of these models for our surveys.

Several factors, such as snow depth, absorbing inclusions and algal community structure, affect the spectral signature beneath sea ice, which all determine which wavelengths perform best in that specific area. This is not the first time when previously reported NDIs have been applied to a different region without success. The same NDI combination 472:485 nm reported Mundy et al. (2007) explained up to 89 % in their study but showed varying performance when applied to sites at two regions in Antarctica, where the same combination explained between 32 % and 79 % of the variance in biomass (Melbourne-Thomas *et al.*, 2015). The same challenge can be seen in this study, as the same NDI combination by Mundy et al. (2007) explained 37 % of biomass variance. This emphasizes the importance of determining a region-specific combination, where all other factors influencing the spectral signature can be considered.

There have been several different NDI combinations reported across the Arctic and Antarctic (e.g. Campbell *et al*., 2014; Forrest *et al*., 2019; Lange *et al.*, 2016; Melbourne-Thomas *et al.*, 2015; Mundy *et al.*, 2007). The studies by both Mundy et al. (2007) and Campbell et al. (2014) were conducted on land-fast FYI in Resolute Bay in Canada, while the study by Lange et al. (2016) also included pack-ice FYI and MYI and different types of snow covers and ice properties. While most reported NDI combinations have been close to the first chl *a* absorption peak, a few studies have reported combinations within the same range as the combinations reported here for the Svalbard sites (Mundy *et al.*, 2007; Lange *et al.*, 2016). All studies, however, have identified different optimal NDIs for each study area, and there has not yet been reported one combination or range of wavelengths that work globally.

Most studies have used transmitted irradiance (µmols photons m^{-2} s^{-1}) or transmittance (%), while this is the first study, to our knowledge, to include standardized radiance. Although the performance of the models based on standardized radiance exhibited the highest correlations with chl *a*, application of the model for investigating spatial variability of chl *a* across a UHI survey, led to grainy and inaccurate images of the distribution across the sub-surface of the ice (**Fig. 5b**). The application of the NDI models based on transmittance, however, for remotely estimating chl *a*, clearly represented the patchiness of sea ice algae growing on the bottom of the ice (**Fig. 5d)** Therefore, NDIs should be constructed using transmittance instead of standardized spectra to remotely estimate chl *a* and spatial variability in sea ice. Transmittance can be obtained either through installing a sensor at the surface of the ice or by extracting the

spectra from an ice free area (e.g. core hole) at the same depth as the under-ice sensor. Using transmittance will account for incident solar radiation, taking into account the influence by clouds or a clear sky (Lange *et al.*, 2016).

Our study empasized the importance of determining area-specific NDI wavelenght combinations for estimating chl *a* biomass. We presented optimal NDIs suitable for two Svalbard fjords pooled together and successfully applied experimentally derived NDI combinations for said fjords. Our optimal NDI combinations were all centered around the red area of the spectrum, due to the thin snow cover in our Svalbard study sites and absence of snow in our laboratory experiments. While NDI combinations centered around the second absorption peak of chl *a* performed best in this comparison, the effect of snow must be excluded with snow depths higher than 0.1 m due to the absorption by snow above 570 nm.

5.5 Conclusion and future work

Through this study, we have demonstrated the potential of using UHI systems and NDIs for estimating and characterizing chl *a* biomass distribution across spatial scales. This study provides an advancement for remote sensing of sea ice algae, by combining existing methods for bio-optical modelling, typically used with sensors with a larger footprint, with high spatial resolution of transmitted light. The UHI can therefore capture the considerable small-scale variability of a few millimeters and centimeters, that cannot be captured by ice coring alone. Optimal NDIs constructed in a controlled laboratory settings were successfully applied to a field community of similar species composition.

Under-ice remote sensing still requires extensive research effort and development of robust bio-optical models for quantifying biomass across the subsurface of the ice. Considering the effect of the optical properties of snow and ice as well as the accessory pigments present is needed for producing a robust NDI-based algorithm. Development of under-ice bio-optical models is a much-needed step towards better understanding of sea ice algal phenology and distribution. Although no global NDI has been determined yet, enough data from different regions might provide a certain range of NDI wavelengths that is applicable to different regions.

5.6 REFERENCES

Arrigo, K.R. and van Dijken, G.L. (2015) 'Continued increases in Arctic Ocean primary production', *Synthesis of Arctic Research (SOAR)*, 136, pp. 60–70. Available at: https://doi.org/10.1016/j.pocean.2015.05.002.

Campbell, K. *et al.* (2014) 'Remote estimates of ice algae biomass and their response to environmental conditions during spring melt', *Arctic*, pp. 375–387.

Campbell, K. *et al.* (2015) 'Characterizing the sea ice algae chlorophyll a–snow depth relationship over Arctic spring melt using transmitted irradiance', *Journal of Marine Systems*, 147, pp. 76–84.

Campbell, K. *et al.* (2022) 'Monitoring a changing Arctic: Recent advancements in the study of sea ice microbial communities', *Ambio*, 51(2), pp. 318–332.

Cimoli, E., Meiners, K.M., *et al.* (2017) 'Spatial variability in sea-ice algal biomass: an under-ice remote sensing perspective', *Advances in Polar Science*, 28(4), pp. 268–296.

Cimoli, E., Lucieer, A., *et al.* (2017) 'Towards improved estimates of sea-ice algal biomass: experimental assessment of hyperspectral imaging cameras for under-ice studies', *Annals of Glaciology*, 58(75pt1), pp. 68–77. Available at: https://doi.org/10.1017/aog.2017.6.

Fernández-Méndez, M. *et al.* (2015) 'Photosynthetic production in the central Arctic Ocean during the record sea-ice minimum in 2012', *Biogeosciences*, 12(11), pp. 3525–3549.

Forrest, A.L. *et al.* (2019) 'Exploring Spatial Heterogeneity of Antarctic Sea Ice Algae Using an Autonomous Underwater Vehicle Mounted Irradiance Sensor', *Frontiers in Earth Science*, 7. Available at: https://www.frontiersin.org/article/10.3389/feart.2019.00169 (Accessed: 11 April 2022).

Fransson, A. *et al.* (2015) 'Effect of glacial drainage water on the CO 2 system and ocean acidification state in an A rctic tidewater-glacier fjord during two contrasting years', *Journal of Geophysical Research: Oceans*, 120(4), pp. 2413–2429.

Guillard, R.R.L. and Ryther, J.H. (1962) 'STUDIES OF MARINE PLANKTONIC DIATOMS: I. CYCLOTELLA NANA HUSTEDT, AND DETONULA CONFERVACEA (CLEVE) GRAN.', *Canadian Journal of Microbiology*, 8(2), pp. 229–239. Available at: https://doi.org/10.1139/m62-029.

Jeffrey, S.W., Wright, S.W. and Zapata, M. (2011) 'Microalgal classes and their signature pigments', in C.A. Llewellyn et al. (eds) *Phytoplankton Pigments: Characterization, Chemotaxonomy and Applications in Oceanography*. Cambridge: Cambridge University Press (Cambridge Environmental Chemistry Series), pp. 3–77. Available at: https://doi.org/10.1017/CBO9780511732263.004.

Kohlbach, D. *et al.* (2016) 'The importance of ice algae-produced carbon in the central Arctic Ocean ecosystem: Food web relationships revealed by lipid and stable isotope analyses', *Limnology and Oceanography*, 61(6), pp. 2027–2044. Available at: https://doi.org/10.1002/lno.10351.

Kohlbach, D. *et al.* (2017) 'Strong linkage of polar cod (Boreogadus saida) to sea ice algae-produced carbon: Evidence from stomach content, fatty acid and stable isotope analyses', *Progress in Oceanography*, 152, pp. 62–74. Available at: https://doi.org/10.1016/j.pocean.2017.02.003.

Lange, B.A. *et al.* (2016) 'Sea ice algae chlorophyll a concentrations derived from under-ice spectral radiation profiling platforms', *Journal of Geophysical Research: Oceans*, 121(12), pp. 8511–8534. Available at: https://doi.org/10.1002/2016JC011991.

Lange, B.A. *et al.* (2017) 'Characterizing Spatial Variability of Ice Algal Chlorophyll a and Net Primary Production between Sea Ice Habitats Using Horizontal Profiling Platforms', *Frontiers in Marine Science*, 4. Available at: https://www.frontiersin.org/article/10.3389/fmars.2017.00349.

Lannuzel, D. *et al.* (2020) 'The future of Arctic sea-ice biogeochemistry and ice-associated ecosystems', *Nature Climate Change*, 10(11), pp. 983–992. Available at: https://doi.org/10.1038/s41558-020-00940-4.

Legendre, L. *et al.* (1992) 'Ecology of sea ice biota', *Polar Biology*, 12(3), pp. 429–444. Available at: https://doi.org/10.1007/BF00243114.

Legendre, L. and Gosselin, M. (1991) 'In situ spectroradiometric estimation of microalgal biomass in first-year sea ice', *Polar Biology*, 11(2), pp. 113–115. Available at: https://doi.org/10.1007/BF00234273.

Leu, E. *et al.* (2015) 'Arctic spring awakening – Steering principles behind the phenology of vernal ice algal blooms', *Progress in Oceanography*, 139, pp. 151–170. Available at: https://doi.org/10.1016/j.pocean.2015.07.012.

Lund-Hansen, L.C. *et al.* (2017) 'Is colonization of sea ice by diatoms facilitated by increased surface roughness in growing ice crystals?', *Polar Biology*, 40(3), pp. 593–602. Available at: https://doi.org/10.1007/s00300-016-1981-3.

Lund-Hansen LC *et al.* (2020) 'Effects of increased irradiance on biomass, photobiology, nutritional quality, and pigment composition of Arctic sea ice algae', *Marine Ecology Progress Series*, 648, pp. 95–110.

Martín *et al., in prep.* 'Species specific growth rates of sea ice diatoms in relation to different light levels

Meiners, K.M. *et al.* (2017) 'Antarctic pack ice algal distribution: Floe-scale spatial variability and predictability from physical parameters', *Geophysical Research Letters*, 44(14), pp. 7382–7390. Available at: https://doi.org/10.1002/2017GL074346.

Melbourne-Thomas, J. *et al.* (2015) 'Algorithms to estimate Antarctic sea ice algal biomass from under-ice irradiance spectra at regional scales', *Marine Ecology Progress Series*, 536, pp. 107–121.

Miller, L.A. *et al.* (2015) 'Methods for biogeochemical studies of sea ice: The state of the art, caveats, and recommendations', *Elementa: Science of the Anthropocene*. Edited by J.W. Deming and S.F. Ackley, 3, p. 000038. Available at: https://doi.org/10.12952/journal.elementa.000038.

Moreau, S. *et al.* (2016) 'Assessment of the sea-ice carbon pump: Insights from a three-dimensional ocean-sea-ice biogeochemical model (NEMO-LIM-PISCES) Assessment of the sea-ice carbon pump', *Elementa: Science of the Anthropocene*, 4.

Mundy, C.J. *et al.* (2007) 'Influence of snow cover and algae on the spectral dependence of transmitted irradiance through Arctic landfast first-year sea ice', *Journal of Geophysical Research: Oceans*, 112(C3). Available at: https://doi.org/10.1029/2006JC003683.

Neukermans, G., Oziel, L. and Babin, M. (2018) 'Increased intrusion of warming Atlantic water leads to rapid expansion of temperate phytoplankton in the Arctic', *Global Change Biology*, 24(6), pp. 2545–2553.

Nicolaus, M. *et al.* (2012) 'Changes in Arctic sea ice result in increasing light transmittance and absorption', *Geophysical Research Letters*, 39(24). Available at: https://doi.org/10.1029/2012GL053738.

Nilsen, F. *et al.* (2008) 'Fjord–shelf exchanges controlled by ice and brine production: the interannual variation of Atlantic Water in Isfjorden, Svalbard', *Continental Shelf Research*, 28(14), pp. 1838–1853.

PARSONS, T.R., MAITA, Y. and LALLI, C.M. (1984) '4.3 - Fluorometric Determination of Chlorophylls', in T.R. PARSONS, Y. MAITA, and C.M. LALLI (eds) *A Manual of Chemical & Biological Methods for Seawater Analysis*. Amsterdam: Pergamon, pp. 107–109. Available at: https://doi.org/10.1016/B978-0-08-030287-4.50034-7.

Perovich, D.K. *et al.* (1993) 'Bio-optical observations of first-year Arctic sea ice', *Geophysical Research Letters*, 20(11), pp. 1059–1062. Available at: https://doi.org/10.1029/93GL01316.

Post, E. (2017) 'Implications of earlier sea ice melt for phenological cascades in arctic marine food webs', *Food Webs*, 13, pp. 60–66. Available at: https://doi.org/10.1016/j.fooweb.2016.11.002.

Tran, N.H., Hu, J. and Ong, S.L. (2013) 'Simultaneous determination of PPCPs, EDCs, and artificial sweeteners in environmental water samples using a single-step SPE coupled with HPLC–MS/MS and isotope dilution', *Talanta*, 113, pp. 82–92.

Vancoppenolle, M. *et al.* (2013) 'Role of sea ice in global biogeochemical cycles: emerging views and challenges', *Quaternary science reviews*, 79, pp. 207–230.

Zhang, H. *et al.* (2018) 'Estimation of phytoplankton taxonomic groups in the Arctic Ocean using phytoplankton absorption properties: Implication for ocean-color remote sensing', *Optics Express*, 26(24), pp. 32280–32301.

Zhuang, Y. *et al.* (2021) 'Freshening leads to a three-decade trend of declining nutrients in the western Arctic Ocean', *Environmental Research Letters*, 16(5), p. 054047.

6. CHAPTER 4: APPLICATION OF HYPERSPECTRAL IMAGERY COMBINED WITH NDIS FOR ESTIMATING SEA ICE ALGAL CHL A BIOMASS, PRODUCTION AND PIGMENT COMPOSITION

6.1 INTRODUCTION

Under-ice remote sensing methods for mapping the bio-optical characteristics of sea ice are becoming increasingly used by the scientific community, providing a non-destructive method for mapping sea ice algal distribution. Most studies, including Chapter 2 of this thesis, have focused on remotely estimating chlorophyll *a* (chl *a*) across the sea ice subsurface by relating under-ice irradiance and transmittance to destructively measured chl *a* concentration via bio-optical models that use transmitted irradiance or transmittance ratios or Normalised difference indices (NDIs) (Legendre and Gosselin, 1991; C. J. Mundy *et al.*, 2007). Recent advances in the development of NDIs have been made by assessing region-specific wavelength combinations across the Arctic and Antarctic (e.g., Campbell et al., 2014; Forrest et al., 2019; Melbourne-Thomas et al., 2015; Wongpan et al., 2018), as well the application of NDIs for analyzing spatial variability of sea ice algal biomass (Lange *et al.*, 2016) or sea ice algal photophysiology (Campbell *et al.*, 2022).

The objective of this chapter is to build off of the NDI model obtained in chapter two by exploring the potential applications of the NDIs for estimating i) sea ice algal accessory pigments and ii) net community production (NCP) in two contrasting Svalbard fjords.

6.1.2 REMOTELY ESTIMATING NET COMMUNITY PRODUCTION

Applications of the under-ice spectra for the identification of biological parameters beyond chl *a* shows great potential, as demonstrated by Campbell et al. (2022), where NDI-derived chl *a* values were combined with laboratory-based O_2 measurements to estimate the spatial and temporal variability of *in situ* net community production across a 22,500 m^2 ice floe in the High Arctic. Specifically, O_2- based photosynthesis-irradiance (PI) models were applied to the *in situ* under-ice spectra measured by an ROV, and extrapolated to show variability of NCP across the

sea ice sub-surface. The results demonstrated for the first time net heterotrophic conditions (i.e. conditions of O2 uptake) across both FYI and MYI types (Campbell *et al.*, 2022). Building off of this, it follows that combining the higher resolution data provided by an under-ice hyperspectral imager (UHI) with such incubation derived production models could further improve the fine scale spatio-temporal variability of net community production, e.g. potentially caused by brine channel features (Mundy et al., 2007), and heterotrophy in sea ice environments.

6.1.3 Remotely estimating sea ice algal pigment composition

Remotely identifying and quantifying sea ice algal accessory pigments and their respective *in situ* concentrations based on sub-ice transmitted light has not yet been successfully completed to date. This is predominantly due to the fact that pigment processing is expensive and time-consuming and the differentiating between the influence of different pigments on the spectra is difficult. However, incorporating pigment estimates into currently used bio-optical models could, for example, give insight of the functional groups present (e.g. diatoms vs. flagellate cells) due to the known variability in pigment ratios between a number of functional groups (Jeffrey, Wright and Zapata, 2011). For example, fucoxanthin is widely found in diatoms and some dinoflagellates, while peridinin can be used for certain types of dinoflagellates (Higgins, Wright and Schlüter, 2011; Jeffrey, Wright and Zapata, 2011). In polar waters, where Zeaxanthin is not common in sea ice algae, it can indicate the presence of bacteria (Higgins, Wright and Schlüter, 2011). In addition, pigments related to algal stress responses, such as xanthophylls that are produced under conditions of harmful high-light levels or light-harvesting carotenoids produced in low light conditions to support greater light absorption, could therefore indicate the physiological state of the algae present (Brunet *et al.*, 2011). The influence of accessory pigments might also affect the error of bio-optical models estimating chl *a* biomass, as the effect of other pigments on the spectra often overlaps and thus cannot be entirely excluded (Cimoli *et al.*, 2017) . Incorporating pigments into a bio-optical model, that is not only reliable, but relatively effective, is not a trivial task. The overlap of absorption peaks between accessory pigments themselves is considerable (Chapter 1; **Fig 4**), making it difficult to differentiate their effect on the spectral signature measured beneath sea ice. In addition, the actual energy absorbed by each molecule of pigment is not constant, and also changes as a function of environment, such differences light field where certain wavelengths are stronger than others in e.g. different depths of the ocean or as a result of absorbents in the ice (Johnsen *et al.*, 2011).

Building off of work in Chapter two where a UHI was deployed under the sea ice of two contrasting Svalbard fjords in order to establish an optimal NDI and map ice algal chl *a* distribution, here we combine this model with O_2-based measurements following Campbell et al. (2022) and map the variability of chl a -specific production from a scale of sub-millimeter to several meters. Additionally, the use of hyperspectral imagers for the quantification of sea ice algal accessory pigments and functional groups is also be investigated.

6.2 Materials and methods

The description and location of the Svalbard sampling sites are detailed in section 5.4. Briefly, two environmentally contrasting Svalbard fjords, Tempelfjorden and Van Mijenfjorden were sampled in April 2022. The environmental conditions in Tempelfjorden are influences by the inflow of Atlantic water as well as a tide-water glacier, while the inflow of Atlantic water is more restricted in Van Mijenfjorden because of the island Akseløya at the sill of the fjord.

6.2.2 Application of NDIs for estimating accessory pigments

To investigate the potential of obtaining potential NDI combinations for the estimation of accessory pigments, the concentrations of a total of 6 pigments relative to chl *a* were examined for the cultured algae of VMC. This culture was chosen based on having the strongest correlation with core-based chl *a* of the chl *a* NDI (650:664 nm) and the strongly evident change in accessory pigment to chl *a* ratio throughout the experimental period. Fucoxanthin was chosen as the main pigment of interest within this chapter based on the following observations: 1) its absorption range of 450-550 nm had minimal overlap with chl *a*, thus minimising overlap of the two pigments on the spectra; 2) the concentration of fucoxanthin was significant, representing 35 % of total pigment concentration throughout the experiment (n=10), and between 53 % and 82 % compared to the chl *a* concentration; and 3) the high concentration of fucoxanthin relative to chl *a* changed as the experiment progressed, allowing a comparison of the effect on the spectral absorption between a high fucoxanthin compared to chl *a* (average 75 % of total chl *a*) and a low fucoxanthin compared to chl *a* (average 55 % of total chl *a*).

Hereafter, the high fucoxanthin compared to chl *a* (75 %) will be addressed as high fucoxanthin, and low fucoxanthin compared to chl *a* (55 %) as low fucoxanthin.

Due to the low concentration and overlap of the absorption ranges of fucoxanthin with other pigments (Chapter 2; **Fig. 4.)**, the application of the NDI approach here will focus on fucoxanthin only while other pigments will be discussed.

Following the process of obtaining an optimal NDI combination for chl *a*, correlation matrices of all possible wavelength combinations and measured fucoxanthin concentrations were constructed based on transmittance.

Normalized difference indices (NDI) were calculated according to the following equation:

$$NDI = [T(\lambda 1) - T(\lambda 2)] / [T(\lambda 1) + T(\lambda 2)],$$

where T(λx) represent transmittance at a given wavelength. Calculations were performed on wavelengths within the range of 381-750 nm to capture the variability within the range of PAR. Pearson correlation surfaces were constructed to examine all possible NDI wavelength combinations and the correlation with measured fucoxanthin concentration for transmittance. Two correlation matrices were created, one for high fucoxanthin and one for low fucoxanthin, but the optimal NDI combination was chosen using the high fucoxanthin and applied to the low fucoxanthin. The optimal NDI for fucoxanthin was chosen based on three main criteria 1) correlation factor 2) within the absorption range of fucoxanthin, between 450-550 nm, 3) outside of the two absorption peaks of chl *a* (around 440 nm and 670 nm). A distance of a minimum 10 nm between the two chosen wavelengths was kept to avoid artificial correlation between neighbouring wavelengths. The correlation values for the chosen wavelengths were compared between low and high fucoxanthin.

6.2.3 O_2 OPTODE INCUBATIONS AND DETERMINATION OF FJORD SPECIFIC NCP

The NCP was determined for TF1 and VM1 using the O_2 optode method developed by Campbell et al. (2016). These sites were chosen because of their contrasting biomass (Chapter 3; **table 1**) and species composition (Section 5.4.3.1). The O_2 optode incubation method includes incubating the melted ice core samples, pooled together for each site, in airtight borosilicate glass bottles across a range of light intensities ranging from 0 to approximately 250 µmol m^2 s^{-1}. Continuous measurements of dissolved O_2 were measured with Firesting oxygen optodes, from which the relative change in dissolved O_2 was calculated. Pseudo-duplicate samples of chl *a* were collected prior to the incubations (T_0) and filtered onto 25-mm GF/F filters (Whatman), which were then placed in 90 % acetone for 18-24 h for pigment extraction. The average chl *a* was determined before and after acidification using a fluorometer (Turner Designs Trilogy Fluorometer; Parsons et al., 1984). P-I relationships were determined by K. Campbell as chl *a* specific NCP versus incubation light intensity, using the exponential equation of Platt, 1980 without the influence of photoinhibition. An extensive description of the method and equation can be found in Campbell et al. (2016). The site-specific NCP was determined by calculating the light specific production value per chl *a* (µg/L^{-1}) for the average integrated PAR (µmol m^2 s^{-1}). The production value was then multiplied by the per pixel chl *a* image values (µg/L^{-1}) to obtain the variability of total NCP across the subsurface of the ice.

6.3 RESULTS AND DISCUSSION

6.3.2 PHYSICAL AND BIOLOGICAL SVALBARD SITE CHARACTERISTICS

Environmental characteristics are summarized in Chapter 3; **Table 1**. Snow and ice thickness varied across all sites, with the thickest snow (12.5 ± 2 cm) at VM1 and thickest ice at VM2 (40.71 ± 1.27 cm) measured at VM1. The thinnest snow was measured at VM2 (3 ± 0) and thinnest ice at TF1 (31.6 ± 0.47). Lowest integrated PAR was measured at VM1 (0.42 ± 0.08) and highest at TF1 (2.82 ± 0.09). The lowest chl *a* concentrations were measured at TF1 (0.39 ± 0.13 mg/m^{-2}), while substantially higher concentrations were measured at VM1 (6.58 ± 0.71 mg/m^{-2}; Table 1). The ice algal communities of all sites were dominated by pennate diatoms, with an average proportion of 97.5 % at VM1 and VM2, and 66 % at TF1, where the remaining 34 % mostly composed of different flagellates (Forgereau et al., *in prep*).

6.1.2 APPLICATION OF NDI MODEL FOR CHL A BIOMASS DISTRIBUTION

By applying the optimal NDI model (650:664 nm, R^2=0.97, n=11) for the Svalbard sites based on transmittance, obtained in Chapter 2, to the under-ice spectra collected at TF1 and VM1, bottom-ice chl *a* biomass distribution was estimated for these sites. Images of the subsurface of the ice were constructed of the NDI-derived chl *a* biomass distribution, where chl *a* concentration (mg/m^{-2}) was estimated per image pixel, a scale of 0.5 mm x 0.5 mm (**Fig. 1**). From here on, these images will be referred to as Chl *a* images.

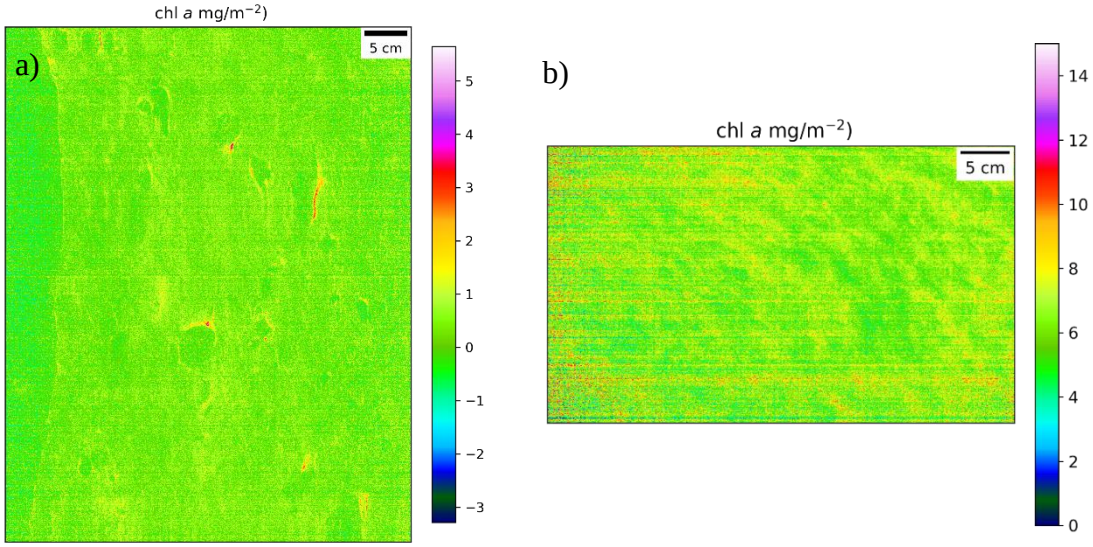

Figure 1. Chl *a* images calculated based on the NDI(650:664 nm)-derived chlorophyll *a* (mg/m^2) distribution under landfast ice in a) low biomass TF1, and b) high biomass VM1.

The chl *a* images show a clear difference between sites representing low and high biomass. As seen in the TF1 image (Figure 1a), the chl *a* distribution show areas of accumulated algae (red color), with concentrations up to 2 mg/m^{-2}, while the average concentration is below 0.4 mg/m^{-2}. The layer of algae was loosely attached to a fragile skeletal layer at the bottom of the ice, and an area of low or no chl *a* biomass can be seen at the left side of the image. The skeletal layer at VM1 was thicker (~ 2 cm, pers. obs.) and exhibited an algal layer infiltrating into the bottom 2 cm of the ice. In comparison, the chl *a* image for VM1 shows a more even distribution of chl *a* biomass related to TF1 (**Fig. 1).** As expected, however, patches of high and low chl *a* are visible, with differences in chl *a* concentration of up to 6 mg/m^{-2} over a scale of 5 cm.

6.1.3 Application of NDI model for net community production (NCP)

Net community production normalised to chl *a* (mg/m^{-2}) based on average integrated PAR was found to be XX for TF1 (PAR 2.82 µmol m^2 s^{-1}) and XX for VM1 (PAR 0.42 µmol m^2 s^{-1}).

Despite the differences chl *a* biomass and thickness of the snow cover between sample sites, NCP in relation to average integrated PAR was found to be consistently heterotrophic (i.e. negative) for both study sites. These observations support previous studies conducted for Arctic FYI, where consistent net heterotrophy was observed in ice floes in the Lincoln Sea (Rysgaard *et al.*, 2008; Campbell *et al.*, 2017, 2022). Production rates related to chl *a* concentration (**Fig. 2**) show higher net consumption of oxygen for areas of higher algal biomass. A comparison between the two sites representing low (TF1) and high (VM1) biomass show higher oxygen consumption relative to chl *a* for TF1 (-0.35 . µmol O_2 µg chl *a* L^{-1} h^{-1} for PAR 2.82 µmol m^2 s^{-1}) compared to VM1 (-0.0019 µmol O_2 µg chl *a* L^{-1} h^{-1} for PAR 0.42 µmol m^2 s^{-1}.

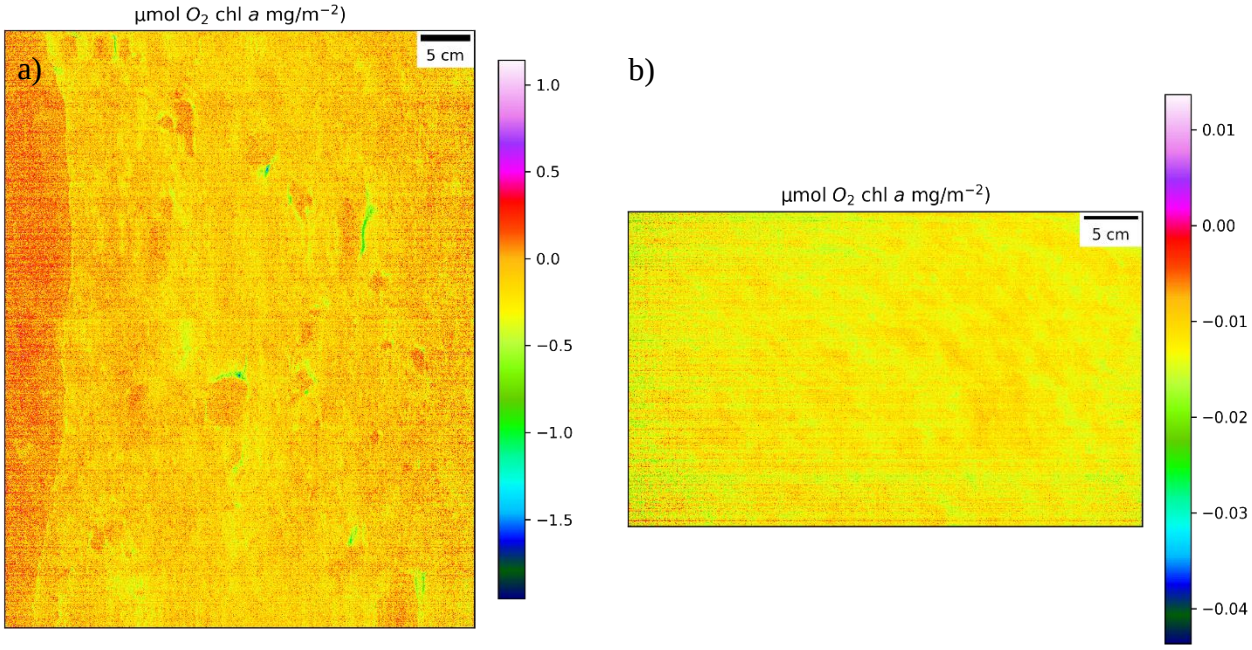

Figure 2. Net community production µmol O_2 µg chl *a* L^{-1} h^{-1} based on average integrated PAR in a) TF1, and b) VM1. Note the different scales on the color bars.

The spatial variability of chl *a* biomass and NCP illustrate captured for both TF1 and VM1 the potential for fine (mm) scale variability within ice algal blooms that can only be captured via remote sensing methods like the use of an UHI. Common methods for sampling, such as coring, cannot capture the spatial variability of biomass small-scale bio-physical interactions on this scale, leading to biased estimates of both biomass and related production. Lange et al. (2017) also highlighted the importance of up-scaling core based chl *a* and production to scales on the

order 100 m to 1000 m and the effectiveness of under-ice profiling platforms in facilitating this. From a comparison between core-based chl *a* and estimates made using an ROV,they demonstrated that core-based estimates of chl *a* (i.e. without the application of remote sensing) did not effectively capture large scale spatial variability or the variability below 2 m.

6.1.4 APPLICATION OF NDI MODEL FOR THE ESTIMATION OF PIGMENT COMPOSITION – VMC

Fucoxanthin had the highest concentration out of all accessory pigments, with a maximum of 42 % of the total pigment concentration (**Fig. 3)**. Due to the low concentration and overlap of the absorption ranges of Fucoxanthin with other pigments (Chapter 2; **Fig. 4)**, the application of the NDI approach here will focus on fucoxanthin only while other pigments will be discussed.

While at the start of the experiment the fucoxanthin to chl *a* ratio was higher, on average 70 % of total chl *a* concentration, fucoxanthin compared to chl *a* concentration decreased to an average of 54 % at the end of the experiment.

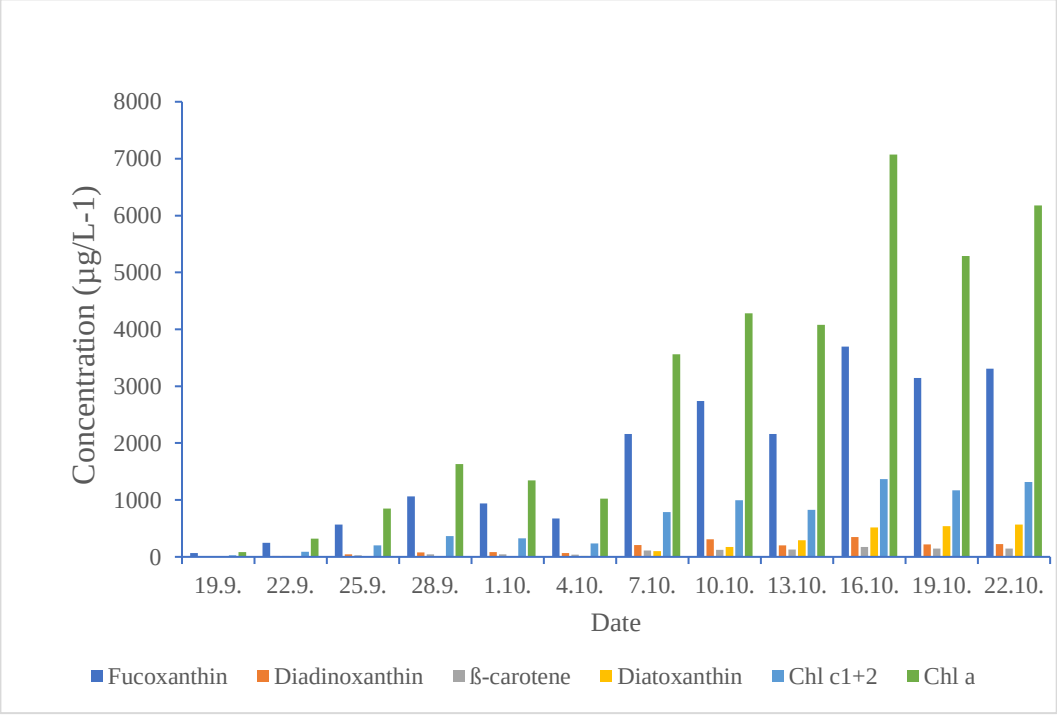

Figure 3. Development of the concentration of all pigments identified in VMC throughout the experiment, compared to measured chl *a* concentration.

The NDI correlation matrices between all possible wavelengths that were constructed for both the start (n=4) and end (n=4) of the experiment show differences in the areas of highest correlation (**Fig. 4**). Following the criteria of choosing a wavelength combination outside of the absorption peaks by chl *a* but within the absorption range of fucoxanthin (450-550 nm), the wavelength combination of NDI (499:509) showed the highest correlation (0.92) for scans 1-4, which had a higher concentration of fucoxanthin compared to chl *a*). The same combination showed lower correlation (0.62) for scans 9-12 (lower fucoxanthin). Simple linear regression was performed for both groups of scans, where the model performed notably better for scans 1-4 (R^2 = 0.85) compared to scans 9-12 (R^2=0.39).

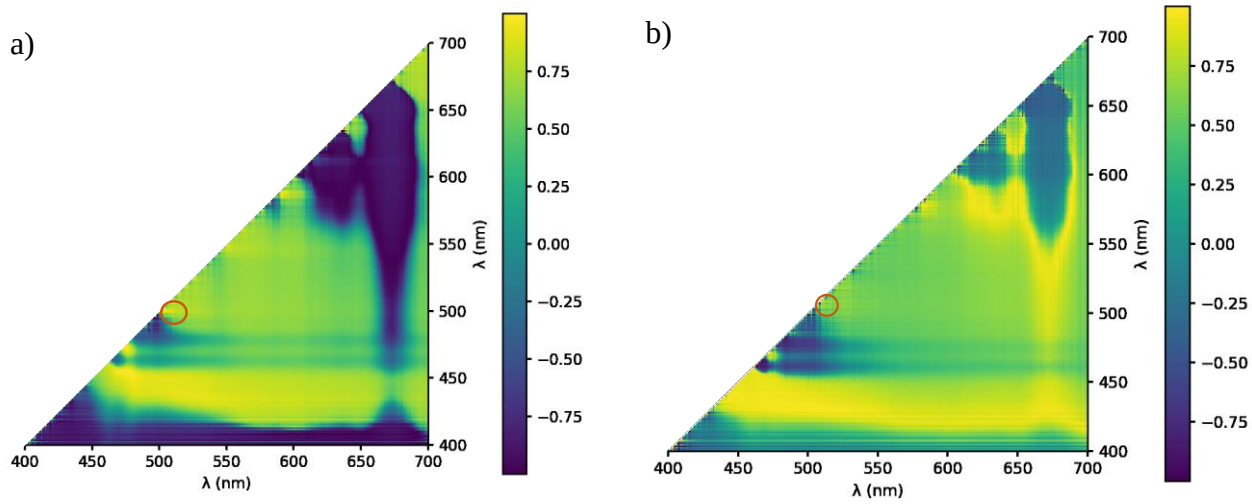

Figure 4. Correlation matrices of all possible NDI wavelength combinations for VMC a) scans 1-4 with high fucoxanthin, and b) scans 9-12 with lower fucoxanthin concentration compared to chl *a*. The area of the chosen NDI combination (499:509 nm) is circled in orange.

The NDI wavelength combination for fucoxanthin (499:509 nm) was applied to all scans for VMC (n=10), where the chosen wavelength combination explained 91 % of fucoxanthin variability (**Fig. 5**).

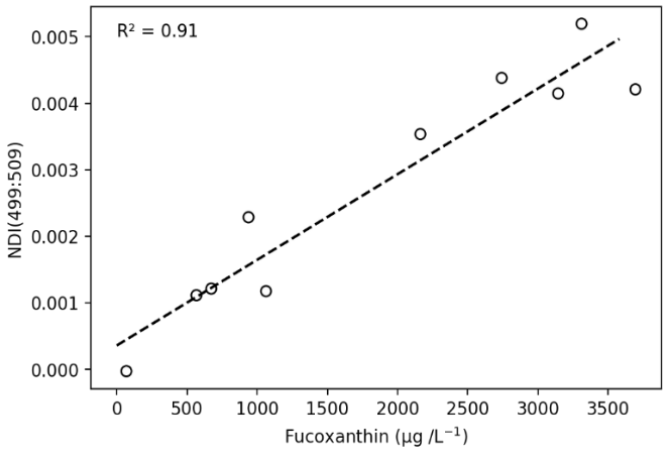

Figure 5. Linear regression for NDI (499:509 nm) for fucoxanthin in a) VMC (R^2=0.91) and, b) EUC (R^2= 0.95).

By applying the NDI to an experimental culture, where all conditions were controlled, other factors than pigments influencing the spectra can be excluded. It is possible that the higher correlation in the correlation matrices around 510 nm (**Fig. 4)** is caused by fucoxanthin, as the

correlation above 500 nm should no longer be affected by chl *a* and the NDI combination is within the absorption of fucoxanthin. Although the low concentration of other accessory pigments compared to fucoxanthin suggest that the signal is, in fact, caused by fucoxanthin, the influence of these pigments cannot be entirely excluded. Many accessory pigments, e.g., diadinoxanthin, β,β-carotene and peridinin, have overlapping ranges of absorption with fucoxanthin (Chapter 2; **Fig. 4**) (Johnsen *et al.*, 2011; Moisan *et al.*, 2017). In addition, the exact absorption of fucoxanthin is not always exact as the weight specific absorption coefficients can vary with e.g. the solvent it is extracted in (Johnsen *et al.*, 2011).

The change in fucoxanthin concentration related to chl *a* in this study could have been a result of either self-shading with increasing biomass or momentary nutrient limitation in between replacing media. The change could also be attributed to a shift in the dominating species. Unfortunately, species composition was not determined at the start and end of this experiment, as it is beyond the scope of this research.

Remotely identifying pigment composition is an important advancement in marine research, as this could serve as a tool for the identification the main functional groups present. This study has shown that fucoxanthin can potentially be identified remotely with a UHI using an NDI that has been calibrated, through sampling, to the area-specific conditions. As fucoxanthin is typical for diatoms, diatom dominated blooms can be differentiated from e.g. flagellate dominated blooms. The method could provide a quantitative way of remotely estimating the functional groups present, which normally requires time consuming taxonomic analysis.

In addition, the ratio of different pigments is linked to the phase of the bloom in the Arctic, with a higher peridinin:chl *a* ratio at the start of the bloom and an increase of the fucoxanthin:chl *a* ratio towards the end of the bloom (**Fig. 6**). This follows the trend of a progression from a flagellates dominated community to a diatom dominated community (Lund-Hansen *et al.*, 2020). Therefore, estimations of the accessory pigment to chl *a* pigment could also indicate the phase of the bloom. Unfortunately, the peridinin:chl *a* ratio was not investigated in this study, as it is beyond the scope of this research.

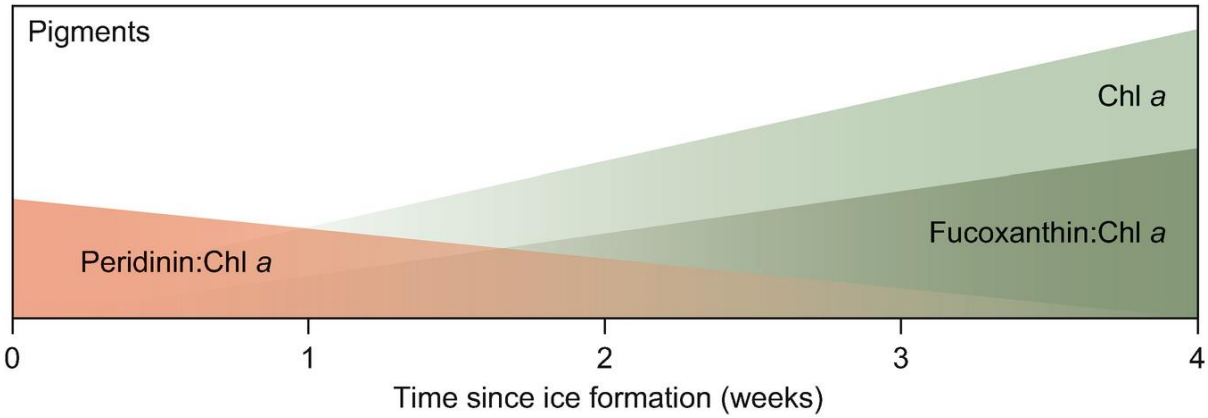

Figure 6. Progression of the pigment ratios for peridinin:chl *a* and fucoxanthin:chl *a* throughout the bloom (Lund-Hansen et al., 2020, modified from Kauko et al., 2018).

Functional groups differ from each other in terms of e.g., growth rates, lipid production and sinking rates, which are also affected by environmental conditions. The proportion of flagellates versus diatoms also affects food availability and quality available for grazing microorganisms at higher trophic levels, as diatoms generally exhibit higher growth rates, higher fatty acid production and faster sinking rates than flagellates, serving as crucial food source and an important link in benthic-pelagic coupling in the Arctic (e.g. Kohlbach et al., 2016).

6.2 Conclusion

Estimates of sea ice algal biomass and related production are often biased due to the inability of traditional sampling methods of capturing fine-scale variability. In this study, NDIs were applied to UHI surveys of two contrasting fjords for remotely estimating chl *a* biomass distribution across the sea ice sub-surface. The results revealed high spatial variability of chl *a* concentration of up to 6 mg/m^2 differences within an area of less than 5 cm, emphasizing the importance of developing remote sensing methods for a more accurate overview of sea ice algal biomass. This spatial variability also translates to large differences in net community production, as demonstrated by this study.

Additionally, the accessory pigment fucoxanthin, an important taxonomic pigment for diatoms, was identified and quantified in controlled laboratory conditions using UHI measurements combined with an optimal NDI specifically determined for fucoxanthin. As the effect of accessory pigments on bio-optical models is apparent, more research effort is needed for the incorporation of said pigments into models used for estimation of biomass.

6.3 References

Brunet, C. *et al.* (2011) 'Pigments and photoacclimation processes', in C.A. Llewellyn et al. (eds) *Phytoplankton Pigments: Characterization, Chemotaxonomy and Applications in Oceanography*. Cambridge: Cambridge University Press (Cambridge Environmental Chemistry Series), pp. 445–471. Available at: https://doi.org/10.1017/CBO9780511732263.017.

Campbell, K. *et al.* (2014) 'Remote estimates of ice algae biomass and their response to environmental conditions during spring melt', *Arctic*, pp. 375–387.

Campbell, K. *et al.* (2017) 'Net community production in the bottom of first-year sea ice over the Arctic spring bloom', *Geophysical Research Letters*, 44(17), pp. 8971–8978.

Campbell, K. *et al.* (2022) 'Net heterotrophy in High Arctic first-year and multi-year spring sea ice', *Elem Sci Anth*, 10(1), p. 00040.

Cimoli, E. *et al.* (2017) 'Spatial variability in sea-ice algal biomass: an under-ice remote sensing perspective', *Advances in Polar Science*, 28(4), pp. 268–296.

Forrest, A.L. *et al.* (2019) 'Exploring Spatial Heterogeneity of Antarctic Sea Ice Algae Using an Autonomous Underwater Vehicle Mounted Irradiance Sensor', *Frontiers in Earth Science*, 7. Available at: https://www.frontiersin.org/article/10.3389/feart.2019.00169 (Accessed: 11 April 2022).

Higgins, H.W., Wright, S.W. and Schlüter, L. (2011) 'Quantitative interpretation of chemotaxonomic pigment data', in C.A. Llewellyn et al. (eds) *Phytoplankton Pigments: Characterization, Chemotaxonomy and Applications*

in Oceanography. Cambridge: Cambridge University Press (Cambridge Environmental Chemistry Series), pp. 257–313. Available at: https://doi.org/10.1017/CBO9780511732263.010.

Jeffrey, S.W., Wright, S.W. and Zapata, M. (2011) 'Microalgal classes and their signature pigments', in C.A. Llewellyn et al. (eds) *Phytoplankton Pigments: Characterization, Chemotaxonomy and Applications in Oceanography*. Cambridge: Cambridge University Press (Cambridge Environmental Chemistry Series), pp. 3–77. Available at: https://doi.org/10.1017/CBO9780511732263.004.

Johnsen, G. *et al.* (2011) 'In vivo bio-optical properties of phytoplankton pigments', in C.A. Llewellyn et al. (eds) *Phytoplankton Pigments: Characterization, Chemotaxonomy and Applications in Oceanography*. Cambridge: Cambridge University Press (Cambridge Environmental Chemistry Series), pp. 496–537. Available at: https://doi.org/10.1017/CBO9780511732263.019.

Kauko, H.M. *et al.* (2018) 'Algal Colonization of Young Arctic Sea Ice in Spring', *Frontiers in Marine Science*, 5. Available at: https://www.frontiersin.org/articles/10.3389/fmars.2018.00199.

Kohlbach, D. *et al.* (2016) 'The importance of ice algae-produced carbon in the central Arctic Ocean ecosystem: Food web relationships revealed by lipid and stable isotope analyses', *Limnology and Oceanography*, 61(6), pp. 2027–2044. Available at: https://doi.org/10.1002/lno.10351.

Lange, B.A. *et al.* (2016) 'Sea ice algae chlorophyll a concentrations derived from under-ice spectral radiation profiling platforms', *Journal of Geophysical Research: Oceans*, 121(12), pp. 8511–8534. Available at: https://doi.org/10.1002/2016JC011991.

Legendre, L. and Gosselin, M. (1991) 'In situ spectroradiometric estimation of microalgal biomass in first-year sea ice', *Polar Biology*, 11(2), pp. 113–115. Available at: https://doi.org/10.1007/BF00234273.

Lund-Hansen, L.C. *et al.* (2020) 'Spring, Summer and Melting Sea Ice', in L.C. Lund-Hansen et al. (eds) *Arctic Sea Ice Ecology: Seasonal Dynamics in Algal and Bacterial Productivity*. Cham: Springer International Publishing, pp. 61–101. Available at: https://doi.org/10.1007/978-3-030-37472-3_4.

Martín *et al., in prep.* 'Species specific growth rates of sea ice diatoms in relation to different light levels

Melbourne-Thomas, J. *et al.* (2015) 'Algorithms to estimate Antarctic sea ice algal biomass from under-ice irradiance spectra at regional scales', *Marine Ecology Progress Series*, 536, pp. 107–121.

Moisan, T.A. *et al.* (2017) 'Satellite Observations of Phytoplankton Functional Type Spatial Distributions, Phenology, Diversity, and Ecotones', *Frontiers in Marine Science*, 4. Available at: https://www.frontiersin.org/article/10.3389/fmars.2017.00189.

Mundy, C. *et al.* (2007) 'Linking ice structure and microscale variability of algal biomass in Arctic first-year sea ice using an in situ photographic technique', *Polar Biology*, 30(9), pp. 1099–1114.

Mundy, C.J. *et al.* (2007) 'Influence of snow cover and algae on the spectral dependence of transmitted irradiance through Arctic landfast first-year sea ice', *Journal of Geophysical Research: Oceans*, 112(C3). Available at: https://doi.org/10.1029/2006JC003683.

Platt, T. and Gallegos, C.L. (1980) 'Modelling primary production', in *Primary productivity in the sea*. Springer, pp. 339–362.

Rysgaard, S. *et al.* (2008) 'Denitrification activity and oxygen dynamics in Arctic sea ice', *Polar Biology*, 31(5), pp. 527–537. Available at: https://doi.org/10.1007/s00300-007-0384-x.

Wongpan, P. *et al.* (2018) 'Estimation of Antarctic Land-Fast Sea Ice Algal Biomass and Snow Thickness From Under-Ice Radiance Spectra in Two Contrasting Areas', *Journal of Geophysical Research: Oceans*, 123(3), pp. 1907–1923. Available at: https://doi.org/10.1002/2017JC013711.

7. THESIS CONCLUSION

Chapter three provides a calibration of UHI-derived transmitted radiance and measured chl *a* concentration for both laboratory and natural fjord systems and highlights the potential of UHIs for estimating fine-scale (mm) chl *a* biomass using NDIs. Although bio-optical models have been used for estimating sea ice algal biomass, previous studies have not been able to map the distribution on scales as small as in this study.

Chapter four builds off of the model developed in chapter three. The results in this chapter emphasizes ability of the combination of UHI surveys and NDI models for estimating both chl *a* biomass and related net community production from mm-scale to inter-fjord variability. The results from this chapter indicate the importance of remote sensing methods for the study of sea ice algae, as traditional sampling methods cannot capture the variability already evident from only a small survey of the underside of the ice. The effect of accessory pigments on bio-optical models was also investigated in chapter four, and successful identification and quantification of the taxonomic marker fucoxanthin from an experimental community was completed using the linear relationship between transmitted radiance and measured fucoxanthin concentration.

This thesis contributed to the development of remote sensing methods for estimating sea ice algal chl *a* biomass variability, production and pigment composition across spatial scales.

8. SUPPLEMENTARY FIGURES

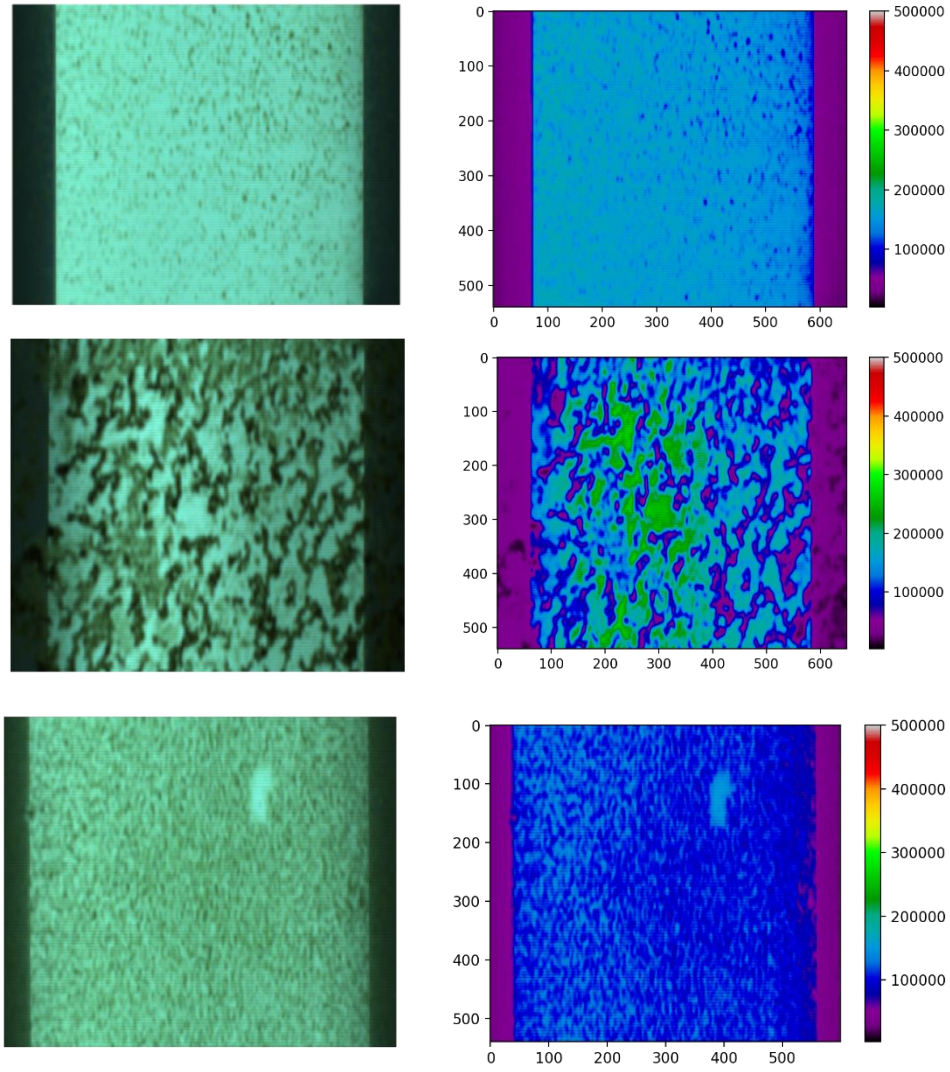

Supplementary Figure 1. RBG composite images and integrated irradiance of all experimental cultures. a) RBG composite of EUC, b) integrated irradiance of EUC, c) RBG composite of ATT, d) integrated irradiance of ATT, e) RGB composite of VMC, f) integrated irradiance of VMC.

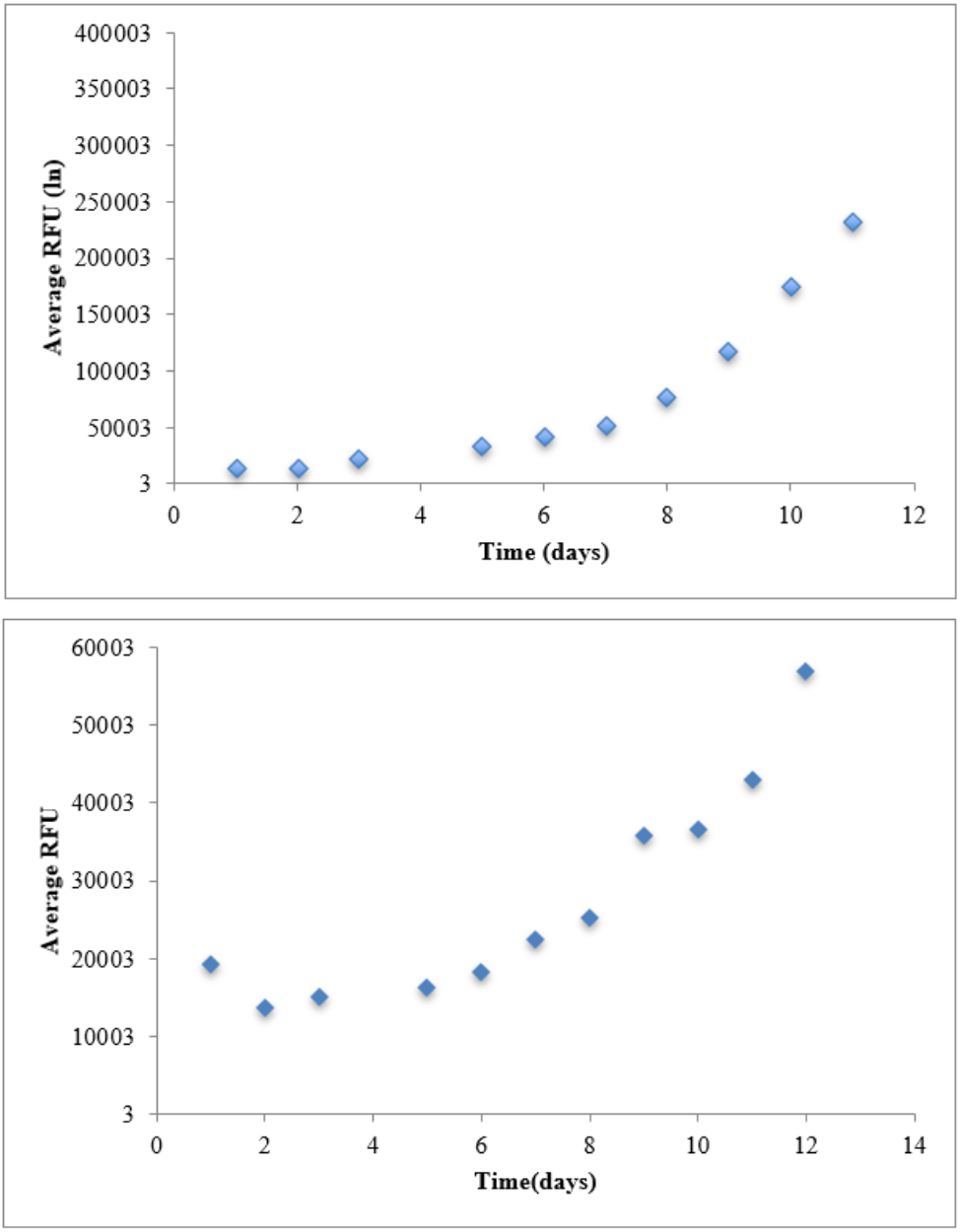

Supplementary figure 2. Growth curves of experimental cultures a) ATT and b) EUC, determined for stock cultures prior to the experiment.

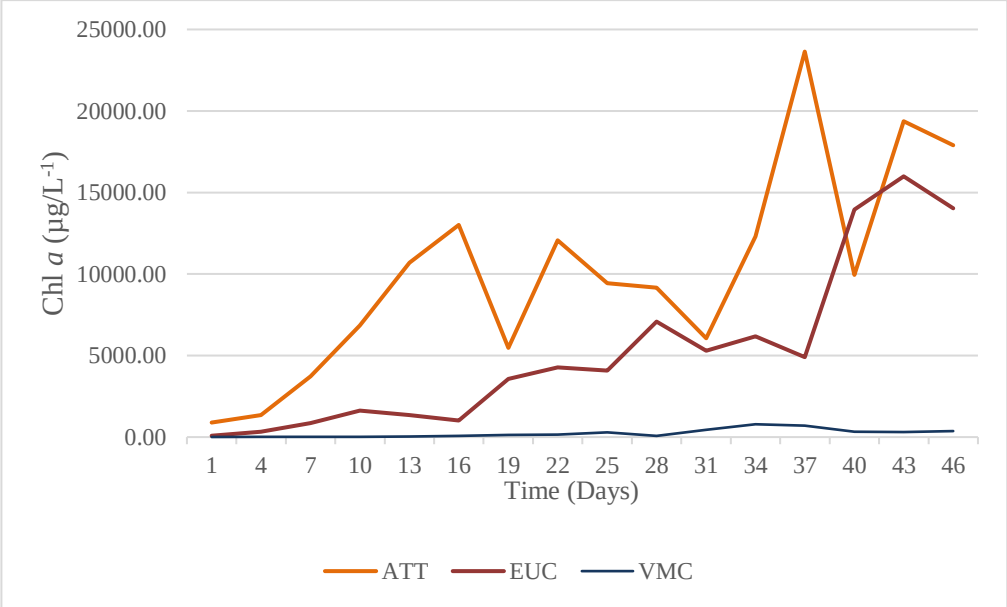

Supplementary figure 3. Measured chl *a* concentration (µg/L-1) for ATT, EUC and VMC during the experimental period.